Eidgenössische Technische Hochschule Zürich
Swiss Federal Institute of Technology Zurich

Optimization of phononic radiation loss patterns in a high overtone bulk acoustic resonator

Master's Thesis

Stefano Marti
`mastefan@ethz.ch`

Laboratory for Solid State Physics
Departement of Physics, D-PHYS
ETH Zürich

Supervisors:
Prof. Dr. Yiwen Chu
Maxwell Drimmer

October 18, 2022

To my family and friends.

Abstract

Loss mechanisms in circuit quantum acousto-dynamic systems (cQAD) are investigated using different simulation methods. COMSOL Multiphysics simulations from which key system parameters can be extracted, such as energy participation ratios and coupling rates, are tested for sensitivity, improved and extended. Furthermore, a novel model to describe a specific type of loss due to electromechanical coupling in the hybrid system is developed, which is based on results extracted from COMSOL as well as from a new approach called the acoustic Schrödinger equation.

Contents

Chapter 1

Introduction

1.1 Quantum information processing

In the advent of the highly active field of quantum information processing (QIP), different quantum platforms including photons [1–3], spins in quantum dots [4], NV centers [5], trapped ions [6], superconducting circuits [7] and phononic systems [8] are being investigated in the search of scalable and high fidelity quantum computing and sensing, each system having advantages and disadvantages. While for example the polarization or the number of photons can be used to encode quantum information robustly, due to their weak interaction with the environment, interaction between photons and hence two-qubit gates are difficult to achieve. Qubits based on the internal energy levels and shared motional states in trapped ions inherently have long coherence times [9] and offer high gate fidelities [10], but comparably slow gate times. Furthermore, increasing the number of ions poses challenges. As a third example, superconducting circuits have relatively low coherence times, only recently surpassed the 500 μs mark in a transmon based on tantalum [11]. However, these circuits can be fabricated according to human-made design choices, providing scalability and opening the door for optimization. Recently, error correcting codes have been implemented on different platforms, as for example the distance-three error correcting code using 17 superconducting qubits [12] or the Gottesman–Kitaev–Preskill (GKP) code on single trapped ions [13], showing potential paths towards fault tolerant quantum computing. Still, many challenges remain to be solved and no particular system is clearly a favorite.

1.2 Hybrid systems: cQAD

One possible solution to the challenges on the road towards fault tolerant computing that has been proposed is to combine different types of quantum systems taking advantage of their intrinsic properties. A promising direction is given by the nascent field of circuit quantum acustodynamics, in which mechanical resonators in the quantum regime and superconducting circuits are coupled [3, 14, 15]. For example, mechanical resonators can be used as long-lived quantum memories [16] due to their high quality factors [17], small device footprints and the fact that cooling different types of mechanical resonators to the groundstate has become possible at GHz frequencies. Apart from quantum memories, phononic systems can also be used for many interesting information processing tasks themselves, as well as for transduction between microwave and optical quantum systems [18, 19] by bridging their wavelength mismatch. Finally, mechanical resonators may offer the possibility to explore fundamental principles of quantum mechanics in sensing applications [20, 21].

1.3 Modeling

Modeling these coupled systems is difficult both analytically and numerically, and no mature methods exists yet. Specifically, the dominant loss channels of such coupled systems must be investigated in order to improve hybrid quantum systems, as experimentally the coherence times are lowered significantly when superconducting circuits and quantum acoustics are combined.

1.4 Goal of this thesis

In this thesis, we investigate different types of simulations with the goal of describing a model for phononic losses in a cQAD device. The work focuses on three types of simulations: solid mechanics simulations based on paraxial beam propagation in a high-overtone bulk acoustic resonators, multiphysics simulations of this resonator coupled to a transmon-like qubit in a 3D microwave cavity as well as simulations based on a new analogy between acoustic modes in a mechanical resonator and solutions of an equivalent Schrödinger equation. From the multiphysics simulations we extract quantities that are combined with the results of this new method, and throughout the thesis, cross-comparison of the used simulations is done.

Chapter 2

Theory

In this thesis, a cQAD device called $\hbar$BAR consisting of a superconducting qubit coupled piezo-electrically to a mechanical resonator in a 3D microwave cavity is investigated. The relevant theoretical framework to model these type of devices is presented in this chapter.

2.1 Modeling superconducting qubits

Different models exist to describe the interactions between superconducting qubits coupled to a common multi-mode cavity, which fall under the field of circuit QED. While theoretically Jaynes-Cummings models can be applied, including higher order cavity modes becomes problematic [22] for practical purposes. Alternatively, semi-classical black box quantization methods [23] allow to determine the Hamiltonian and quality factors of eigenmodes by partitioning the circuit into purely linear and non-linear terms, such that the system properties can be derived from system response simulations. A third approach is the energy participation (EPR) method [24], in which the energies of classical electromagnetic eigenfields are used as a bridge to the quantum description.

2.1.1 Black box quantization

Black box quantization methods allow the computation of the system Hamiltonian in the weak anharmonic limit and are centered on the idea of finding a basis of the linear Hamiltonian part of the superconducting circuit, to which the pure non-linearities are added as perturbations.

In the case of a single Josephson junction coupled to a 3D cavity, the junction is divided into a purely non-linear element, and its linear inductance and capacitance,

$$L_J = \frac{\phi_0^2}{E_J} \tag{2.1}$$

$$C_J = \frac{e^2}{2E_C} \tag{2.2}$$

as can be seen in Figure 2.1.

Here, $\phi_0 = \hbar/(2e)$ is the magnetic flux quantum, e the elementary charge and E_J, E_C denote the Josephson and charging energies, respectively.

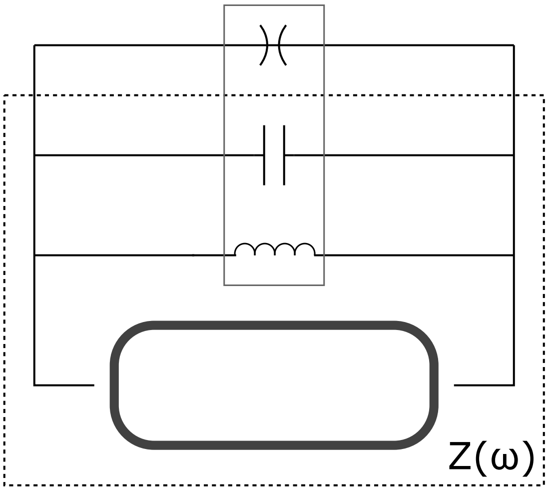

Figure 2.1: Conceptual division in the black box quantization method of a system composed of a Josephson junction (grey box) coupled to a cavity (bold), resulting in a total linear impedance of $Z(\omega)$. The top-most circuit symbol represents the entirely non-linear element of the junction.

The linear junction elements together with the linear electromagnetic environment posed by the cavity can be decomposed into a lumped equivalent Foster circuit (the black box) with the total impedance being a sum of the impedances of each mode p

$$Z(\omega) = \sum_{p=1}^{M} \left(j\omega C_p + \frac{1}{j\omega L_p} + \frac{1}{R_p} \right)^{-1} \tag{2.3}$$

From the linearized circuit, the quality factor of each mode on resonance frequency ω_p can be estimated as

$$Q_p = \frac{\omega_p}{2} \frac{Im[\frac{\partial}{\partial\omega} Y(\omega_p)]}{Re[Y(\omega_p)]} \tag{2.4}$$

which relates to a purcell limited qubit lifetime of $T_1 = Q_p/\omega_p$.

The linear Hamiltonian can be derived from quantizing each mode represented in the impedance $Z(\omega)$ in the canonical way, yielding

$$H_0 = \sum_{p=1}^{M} \hbar\omega_p a_p^\dagger a_p \tag{2.5}$$

Thus, by adding the non-linear element, the total Hamiltonian becomes

$$H = H_0 + H_{nl} \tag{2.6}$$

In the basis of the eigenstates of H_0 the non-linear part can be treated perturbatively.

This procedure can be easily expanded to a circuit including a number of N Josephson junctions, where the total linear impedance will take the form of a $N \times N$ matrix. Therefore, the only remaining question to complete the method for general circuits lies in how to determine the impedance $Z(\omega)$ of the linear circuit as well as its poles (to find the resonance frequencies). This could be achieved by direct measurement, but for prediction of device properties for design and optimization this is not practical. An alternative natural solution is given by means of high frequency structure simulation (HFSS) software such as Ansys HFSS or COMSOL Multiphysics, which solve Maxwell's equations of the system numerically by discretizing the device hosting the circuit in space. However, the needed frequency domain simulations are computationally expensive, as will be illustrated in chapter 3, which is the main disadvantage of black box quantization methods.

A second approach to numerically compute the spectrum of a superconducting circuit without need of frequency domain simulations is the energy participation ratio (EPR) method, which is based on computation of the eigenenergies of the system instead.

2.1.2 EPR method

In this section we review the EPR method [24]. The method is a quantization method based on solutions of a classical finite element method (FEM) simulation. The key idea is that as in black box methods, the system Hamiltonian can be decomposed into a linear and a non-linear part, the former being defined by the eigenfrequencies of the system, while the latter will be found to be defined by the energy participations. Both can be extracted from the simulations. To understand how this is possible, one can derive the system Hamiltonian of a superconducting circuit, quantize it and find this new quantity, the EPR, from which the quantum fluctuation amplitudes can be computed. The procedure starts by computing a spanning-tree of the circuit. The flux in branch j is denoted by ϕ_j, and the vector containing all spanning-tree fluxes by Φ_t. With this, the sum of the energy of all capacitive elements in the circuit can be written in the quadratic form

$$\epsilon_{cap}(\dot{\Phi}_t) = \frac{1}{2}\dot{\Phi}_t^T C \dot{\Phi}_t \tag{2.7}$$

where C is the capacitance matrix of the circuit. The inductive energy on the other hand is composed of a magnetic and kinetic part

$$\epsilon_{ind}(\Phi_t) = \epsilon_{mag}(\Phi_t) + \epsilon_{kin}(\Phi_t) \tag{2.8}$$

where the former is the energy stored in the magnetic fields and reads similarly to equation 2.7

$$\epsilon_{mag} = \frac{1}{2}\Phi_t^T L_{mag}^{-1} \Phi_t \tag{2.9}$$

while the kinetic energy is due to the energy of the electrons in the Josephson junctions of the circuit. This energy that every junction contributes can be divided into a linear and non-linear part

$$\epsilon_j(\phi_j) = \underbrace{\frac{1}{2}E_j(\phi_j/\phi_0)^2}_{\epsilon_j^{lin}(\phi_j)} + \underbrace{E_j\sum_{p=3}^{\infty} c_{jp}(\phi_j/\phi_0)^p}_{\epsilon_j^{nl}(\phi_j)} \tag{2.10}$$

with the second term on the right hand side representing the expansion of the non-linearity. Since the energy of a Josephson junction is

$$\epsilon(\phi_j) = E_J(1 - \cos(\phi/\phi_0)) \tag{2.11}$$

the coefficients in equation 2.10 are

$$c_{jp} = \frac{(-1)^{(p/2+1)}}{p!} \tag{2.12}$$

for even p and zero otherwise. With the capacitive and inductive energies of the system defined, the Lagrangian can be written down as their difference. Again, a partition into a linear and non-linear part is made

$$\mathcal{L}(\Phi_t, \dot{\Phi}_t) = \epsilon_{cap} - \epsilon_{ind} = \mathcal{L}_{lin} + \mathcal{L}_{nl} \tag{2.13}$$

This is done in order to first diagonalize the linear part, after which the non-linear part can be treated as perturbation. For the diagonalization one can use the fact that both the capacitance and inductance matrices are real and symmetric, so they can be diagonalized each with an orthogonal matrix. This gives for the inductance matrix $L = O_L \Lambda O_L^{-1}$, where O_L is orthogonal and Λ diagonal. Therefore, the corresponding energy term becomes

$$\frac{1}{2}\Phi_t^T L^{-1}\Phi_t = \frac{1}{2}\underbrace{(\Phi_t^T O_L \Lambda^{-1/2})}_{\tilde{\Phi}^T} I_L^{-1} \underbrace{(\Lambda^{-1/2} O_L^T \Phi_t)}_{\tilde{\Phi}} \tag{2.14}$$

Here, I_L^{-1} is the identity matrix with inverse dimensions of inductance. Transforming the Lagrangian to the new flux $\tilde{\Phi}$ transforms the capacitance matrix to

$$\tilde{C} = \left(\Lambda^{1/2} O_L^T\right) C \left(O_L \Lambda^{1/2}\right) \tag{2.15}$$

which is also diagonalizable as $O_C^T \tilde{C} O_C = \Lambda I_C$. Applying the same procedure as for the inductance, we finally can write the Lagrangian in diagonal form

$$\mathcal{L}(\Phi_m, \dot{\Phi}_m) = \frac{1}{2}\dot{\Phi}_m^T \Lambda I_C \dot{\Phi}_m - \frac{1}{2}\Phi_m^T I_L^{-1}\Phi_m + \mathcal{L}_{nl}(\Phi_m) \tag{2.16}$$

where Φ_m is the new eigenmode magnetic flux. Applying the Legendre transform to it gives the system Hamiltonian

$$\mathcal{H} = \frac{1}{2} Q_m^T \Omega^2 I_L Q_m + \frac{1}{2} \Phi_m^T I_L^{-1} \Phi_m - \mathcal{L}_{nl}(\Phi_m) \tag{2.17}$$

where $Q_m = \Lambda I_C \dot{\Phi}_m$ is the canonical momentum and Ω the eigenfrequency matrix. Crucially, this eigenfrequency matrix and the corresponding eigenvector matrix can be computed numerically with finite element methods. Now, equation 2.17 is quantized using the canonical Dirac approach, leading to

$$\hat{\mathcal{H}} = \underbrace{\sum_{m=1}^{M} \hbar\omega_m a_m^\dagger a_m}_{H_{lin}} + \underbrace{\sum_{j=1}^{J} \sum_{p=3}^{\infty} E_j c_{jp} \hat{\phi}_j^p}_{\mathcal{H}_{nl}} \tag{2.18}$$

where the quantized dipole flux operator is given as

$$\hat{\phi}_j = \sum_{m=1}^{M} \phi_{mj} (\hat{a}_m + \hat{a}_m^\dagger) \tag{2.19}$$

with the zero point fluctuations (ZPF) ϕ_{mj}. One can then define a quantity called energy participation ratio (EPR) for a mode m and junction j as the ratio of the time averages of the linear energy in the junction to the inductive energy of the mode as

$$p_{mj} = \frac{\overline{\langle \epsilon_{j,lin} \rangle_m}}{\overline{\langle \epsilon_{ind} \rangle_m}} \tag{2.20}$$

where the inductive energy ϵ_{ind} corresponds to half of the total linear energy according to the equipartition theorem. For the expectation, a state with an excitation in mode m is used, but the resulting EPR is in fact independent of the state. The EPR can be extracted from HFSS by computing the eigenmodes of the electromagnetic fields by using the linear inductance L_j and peak current at the junction I_{mj} of eigenmode m,

$$p_{mj} = \frac{1}{2} \frac{L_j I_{mj}^2}{\epsilon_{ind}} \tag{2.21}$$

The key of the EPR method is the following: it can be derived that the energy participation is related to the ZPF as

$$\phi_{mj}^2 = p_{mj} \frac{\hbar\omega}{2E_j} \tag{2.22}$$

Therefore, the energy participation is a parameter that allows the extraction of the quantum fluctuations and with it, $\mathcal{H}_{nl}$. Furthermore, the participations provide insight into losses, as will be explained in the next section.

2.1.3 Losses in superconducting circuits

To date, losses in superconducting qubits are thought to be dominated by close defects acting as a bath of two-level systems (TLS) that couple to the qubits, leading to their decoherence [25, 26]. These defects typically stem from contaminations in the bulk and surface of dielectric materials, and since the type of loss is proportional to the electric field intensity, it is denominated as capacitive. Both bulk and surface dielectric losses can be computed numerically through their corresponding energy participation, which for the former is proportional to the integral of the electric field over its volume V

$$p_{cap,bulk} = \frac{1}{4\varepsilon_{elec}} Re \int_V dv \vec{E}^*_{max} \epsilon \vec{E}_{max} \tag{2.23}$$

where ϵ denotes the dielectric permittivity and ε_{elec} is the total electric field energy. In the case of surface dielectric loss, this is simplified using a spatially constant dielectric permittivity over the surface thickness t.

$$p_{cap,surf} = \frac{t\epsilon}{4\varepsilon_{elec}} Re \int_A ds \left|\vec{E}_{max}\right|^2 \tag{2.24}$$

The sum over the all dielectric elements l leads to the associated capacitive loss

$$\frac{1}{Q_{cap}} = \sum_l \frac{p^l_{cap}}{Q^l_{cap}} \tag{2.25}$$

Apart from dielectric losses, inductive losses can arise from currents in metals at surfaces and in seams, which are proportional to the magnetic field magnitude instead. The former lead to the participation ratios

$$p_{ind,surf} = \frac{\lambda_0 \mu}{4\epsilon} Re \int_A ds |\vec{H}_{max,||}|^2 \tag{2.26}$$

where $\lambda_0(\omega)$ is the frequency dependent skin depth and μ is the magnetic permeability. The participations arising from the interface between two metals (the seam) is similarly

$$p_{ind,seam} = \frac{\lambda_0 t \mu}{4\varepsilon_{mag}} Re \int_A ds |\vec{H}_{max,\perp}|^2 \tag{2.27}$$

for a seam of thickness t. Again, the sum over all elements can be condensed to a total inductive quality factor

$$\frac{1}{Q_{ind}} = \sum_l \frac{p^l_{ind}}{Q^l_{ind}} \tag{2.28}$$

Hence, the total qubit relaxation is a sum of these capacitive and inductive losses

$$\frac{1}{Q_{tot,qb}} = \frac{1}{Q_{cap}} + \frac{1}{Q_{ind}} \tag{2.29}$$

It has to be pointed out again that the first two terms can be extracted from classical eigenmode simulations, making it possible to engineer the geometry of the superconducting circuits to minimize these types of losses.

2.2 Circuit Quantum Acoustodynamics

Analogous to the idea of circuit Quantum Electrodynamics (cQED), in which superconducting circuits are coupled to common electromagnetic modes, the emerging field of circuit quantum acoustic dynamics (cQAD) investigates the interaction between acoustic modes of mechanical resonators and superconducting circuits. This quantum information platform offers many fascinating opportunities and advantages to investigate both fundamental physics and information processing applications. After introducing the basics of waves in solids, the investigated mechanical resonators and different types of losses therein will be described.

2.2.1 Elastic waves

In continuum mechanics, materials can be classified as elastic or inelastic. The former are described by a one-to-one correspondence between stress and strain in the non-piezoelectric solids, whereas for inelastic materials it can be multiple-valued. In its most general form, the elastic relation can be written as the Taylor expansion

$$T_{ij} = T_{ij}(0) + \left(\frac{\partial T_{ij}}{\partial S_{kl}}\right)_{S_{kl}=0} S_{kl} + \frac{1}{2}\left(\frac{\partial^2 T_{ij}}{\partial S_{kl}\partial S_{mn}}\right)_{S_{kl}=S_{mn}=0} S_{kl}S_{mn} + ... \tag{2.30}$$

Keeping only the linear term and using the fact that $T_{ij}(0) = 0$ results in

$$T_{ij} = \alpha_{ijkl} S_{kl} \tag{2.31}$$

where T_{ij} and S_{kl} denote the elements of the second-rank stress and strain tensors, respectively. Because T and S are symmetric, one can rewrite the relationship using the six-vector Voigt notation

$$\tau_i = c_{ij}\epsilon_j \tag{2.32}$$

where c_{ij} denote the elements of the stiffness matrix, which can be found for example in [27]. The dynamics of a solid can be derived from the mass conservation and Newton's second law [28]. The dynamical equation to start with is

$$\rho\frac{\partial^2 u_i}{\partial t^2} = \frac{\partial T_{ij}}{\partial x_j} + f_j \tag{2.33}$$

where ρ denotes the density of the solid, u_i a component of the displacement field and f_j the body forces. Neglecting the body forces f and inserting the ansatz of a monochromatic plane wave with polarization unit vector $\vec{e}$ expressed as

$$\vec{u}(\vec{r}) = u_0 e^{i(\vec{q}\cdot\vec{r}-\omega t)}\vec{e} \tag{2.34}$$

into the dynamical equation leads to the relation

$$\rho\omega^2 e_i = \alpha_{ijlm} q_j q_m e_l \tag{2.35}$$

One can then define the Christoffel tensor as

$$D_{ij} = \frac{1}{\rho}\alpha_{ijlm} q_j q_m \tag{2.36}$$

which depends on the normalized wavevector components q_j, q_m. With this, the dynamical equation can be written as an eigenvalue problem

$$(D_{il} - v^2\delta_{il})e_l = 0 \tag{2.37}$$

While the eigenvalues of this equation correspond to the phase velocity, the eigenvectors represent the polarizations of each of the three plane wave solutions. The largest eigenvalue defines the quasi-longitudinal wave, the other two waves are called quasi-transverse. Since the Christoffel tensor depends on the wavevector, the phase velocity and the wavevector are not necessarily parallel. Furthermore, computing the velocities of a given type of wave for every direction results in a surface called velocity surface. Its inverse, the slowness surface, is a surface of constant frequency $\omega(\vec{q})$. Because the group velocity of the wave is the gradient of the frequency as a function of wavevector, it is normal to the slowness surface. Also, the Poynting vector, defined as

$$P = -\langle v_\phi \cdot T\rangle_t \tag{2.38}$$

becomes

$$P = \frac{1}{2}(\rho\omega^2 u_0^2 c_g)\omega u_0^2 \propto v_g \tag{2.39}$$

for the plane wave ansatz used. Since it is proportional to the group velocity, the energy also flows normal to the slowness surface. For non-isotropic materials, this leads to interesting effects such as phonon focusing due to their non-convex slowness surfaces. For a visual representation of the surfaces, see Figure 2.2.

2.2.2 High overtone bulk acoustic wave resonators (HBAR)

Acoustic waves can be trapped in mechanical resonators analogous to the optical case, resulting in standing waves. For phononic quantum information applications, the coherent control of individual mechanical excitations, phonons, is required, which demands high acoustic quality factor resonators. A figure of merit of practical importance needs to include the resonator frequency, such that often the product $f \cdot Q$ is cited, because it is proportional to the number of coherent oscillations done for a resonator that is

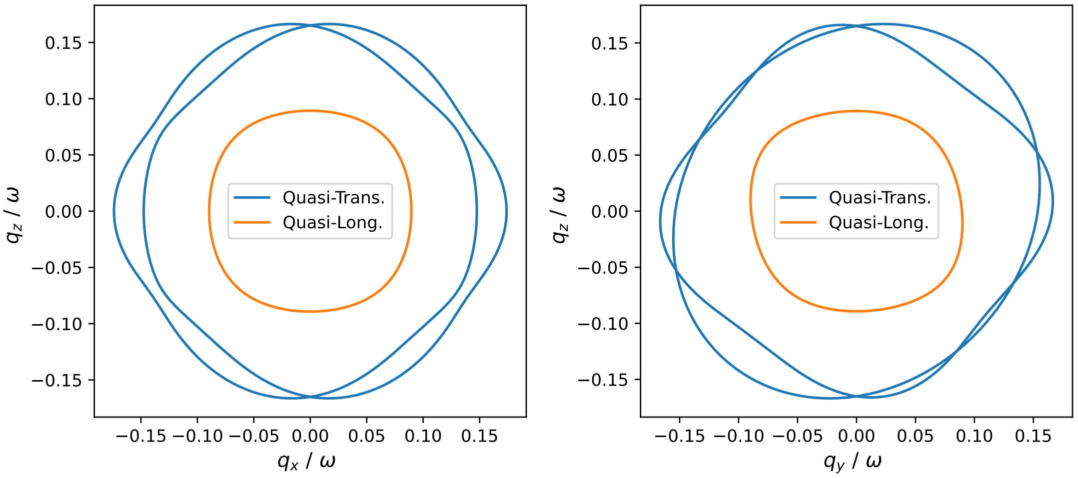

Figure 2.2: Slowness surface cuts for each of the three types of wave in a sapphire crystal. Waves with the smallest wave vectors are denominated quasi-longitudinal, the remaining two quasi-transverse.

coupled to a thermal environment. Although phononic crystal defects with lattice parameters in the micron range and surface acoustic wave resonators (SAW) can achieve high quality factors and are used in quantum information applications, bulk acoustic wave resonators (BAW) have shown to reach record $f \cdot Q$ values of $1.6 \cdot 10^{18}$ at cryogenic temperatures [17]. Another advantage is the size of these BAW resonators, which can be made chip-scale because acoustic wavelengths at GHz frequencies are in the order of 1 μm, and therefore suitable for cQAD experiments. In this thesis, high overtone bulk acoustic wave resonators (HBAR) are investigated, which, as the name implies, support large longitudinal mode numbers. Their properties are analogous to the ones of optical Fabry-Pérot cavities, which are defined by the resonator length and the curvatures of the boundaries forming the mirrors. A central characteristic of such resonators is the free spectral range, i.e. the frequency difference between two longitudinal modes, which is defined as

$$\nu_{FSR} = \frac{v_l}{2L} \tag{2.40}$$

where $v_l = \sqrt{c_{11}/\rho}$ and L denote the longitudinal acoustic velocity and the length of the resonator, respectively. While this is exact for a cavity with two planar surfaces, it is not anymore for curved surfaces and one has to draw on approximations or simulations.

Stability criterion

Modes in HBARs with planar surfaces are unconfined, which can be problematic because it leads to loss due to diffraction. In order to confine the modes, the resonator surfaces have to be curved and fulfill the stability criterion

$$0 \leq \underbrace{\left(1-\frac{L}{\chi R_1}\right)}_{g_1}\underbrace{\left(1-\frac{L}{\chi R_2}\right)}_{g_2} \leq 1 \tag{2.41}$$

with R_1, R_2 being the radii of curvature of the cavity surfaces on either side and the anisotropy parameter being [17]

$$\chi = \frac{v_l^2(v_l^2 - v_t^2)}{v_l^2 v_t^2 - v_t^4 + \gamma^4} \tag{2.42}$$

Here, v_t is the transverse velocity and $\gamma = \sqrt{(c_{12}+c_{44})/\rho}$. In the following, only confined modes will be investigated. Except otherwise indicated, the HBARs will be plano-convex, where the convex surface will be called a *dome*.

Confined modes

In the paraxial approximation, the solutions of the wave equation in a HBAR with infinite spherical surfaces are Laguerre-Gaussian (LG) or Hermite-Gaussian (HG) modes profiles transverse to the paraxial axis and Gaussian along the axis. The LG and HG mode families are the natural solutions in cylindrical and cartesian coordinates respectively and are in fact equivalent, as every LG mode can be written as a sum of HG modes and vice versa [29]. The analytical expression for a Laguerre-Gaussian mode, which appears more often in COMSOL simulations, with azimuthal index l and radial index p in cylindrical coordinates r, ϕ, z is

$$u(r,\phi,z) = A_0 \frac{w_0}{w(z)}\left(\frac{r\sqrt{2}}{w(z)}\right)^{|l|} \exp\left(-\frac{r^2}{w^2(z)}\right) L_p^{|l|}\left(\frac{2r^2}{w^2(z)}\right) \times \tag{2.43}$$

$$\exp\left(-ik\frac{r^2}{2R(z)}\right)\exp(-il\phi)\exp(i\psi(z)) \tag{2.44}$$

with the following quantities:

- w_0 the beam waist at $z = 0$
- $w(z) = w_0\sqrt{1+(\frac{z}{z_R})^2}$ with the Rayleigh length z_R
- $R(z) = \frac{1}{\chi}(z + \frac{z}{z_R^2})$
- $\psi(z) = \arctan\left(\frac{z}{z_R}\right)$

Since the divergence of the acoustic Gaussian beam is given by the Rayleigh length

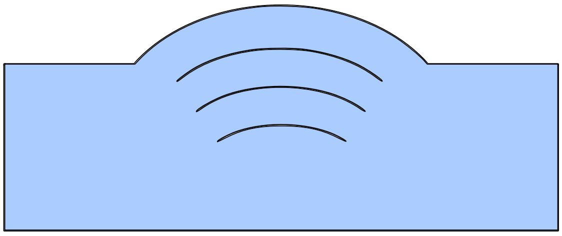

Figure 2.3: Illustration of phase fronts matching the resonator boundaries to meet confinement in a high overtone bulk acoustic resonator (HBAR).

$$z_R^2 = \frac{g_1 g_2 (1 - g_1 g_2)}{(g_1 + g_2 - 2g_1 g_2)^2} \tag{2.45}$$

which for typical samples with resonator lengths $l \approx 420$ μm and dome heights of 1 μm is much longer than the length of the resonator, the paraxial approximation is valid. This can also be observed well in COMSOL simulations done in this parameter regime.

In addition to the free spectral range (FSR), one can look at the spacing between different transverse modes. From the condition that the round-trip phase must be integer multiple of 2π, it follows that this transversal mode spacing is

$$\Delta f = \frac{1}{2\pi} \arctan\left(\frac{L}{z_R}\right) \frac{v_l}{L} \tag{2.46}$$

Confinement can also be understood by looking at the phase fronts of the mechanical modes, which for confinement need to match the reflecting surfaces, see Figure 2.3.

Quantisation

The acoustic modes living in resonators can be quantized following the same procedure as is done with electromagnetic fields. Starting with the normalized mode displacement

$$\vec{u}(\vec{r}, t) = u_0 e^{-i\omega t} \vec{h}(\vec{r}) + c.c \tag{2.47}$$

where the polarization and mode shape are defined by $\vec{h}(\vec{r})$, one can derive that the Hamiltonian of the system composed of the kinetic and potential energy will be

$$\begin{aligned} H &= T + V \quad &(2.48)\\ &= \frac{1}{2}\int dV \frac{\partial u_i}{\partial t}\frac{\partial u_i^*}{\partial t} + \frac{1}{2}\int dV c_{ijlm} \frac{\partial u_i}{\partial x_j}\frac{\partial u_l}{\partial x_m} \quad &(2.49)\\ &= 2\rho\omega^2 |u_0(t)|^2 \quad &(2.50) \end{aligned}$$

Defining the conjugate variables $q = u_0(t) + c.c.$ and $p = -i\omega\rho(u_0(t) + c.c)$

the Hamiltonian can be written in the form of a harmonic oscillator

$$H = \frac{p^2}{2\rho} + \frac{1}{2}\rho\omega^2 q^2 \tag{2.51}$$

to which the canonical quantization can be applied by elevating the conjugate variables to the operators

$$\hat{p} = -i\sqrt{\frac{\rho\hbar\omega}{2}}(a - a^\dagger) \tag{2.52}$$

$$\hat{q} = \sqrt{\frac{\hbar}{2\rho\omega}}(a + a^\dagger) \tag{2.53}$$

so that the quantized displacement is

$$\vec{u}(\vec{r}, t) = \sqrt{\frac{\hbar}{2\rho\omega}}\vec{f}(\vec{r})\hat{a(t)} + H.c. \tag{2.54}$$

2.2.3 Losses in a HBAR

Losses in BAW resonators can either arise from intrinsic properties of the material crystal and its surfaces, or from the resonator geometry. In the following, both will be discussed in more detail.

Intrinsic losses

This type of loss can be ascribed to at least five mechanisms [30].

- Phonons trapped in the resonator can interact and therefore scatter off from each other. The associated quality factor scales with temperature as $Q_{ph-ph} \propto T^{-6.5}$.
- At low temperatures, phonons can also interact with impurity ions in a similar way as qubits with two-level systems (TLS). In this case, theoretically the quality factor depends on the temperature as $Q_{TLS} \propto T^{-1/3}$.
- The third intrinsic loss is attributed to the scattering at the surfaces of the resonator. Since the surfaces can not be made perfect in fabrication, some surface roughness remains. A surface of variance σ^2 has the reflection coefficient $R = e^{-2k^2\sigma^2}$ for a given wavevector k and it can be shown that the randomized wavevectors result for the n-th overtone in the associated Q-factor

  $$Q_{scatt} = \frac{t^2}{2n\sigma^2} \tag{2.55}$$

  For example, in the case of of HBARs with dome thickness $t \approx 420$ μm at overtone $n \approx 100$ and with a surface roughness $\sigma \approx 0.2$ nm, one has $Q_{scatt} \approx 8.8 \cdot 10^{10}$.

- A last mechanism describes loss due to thermal conduction, which results in an effective attenuation of the acoustic wave.

  The losses in a HBAR can be added and therefore the total intrinsic loss is lower-bounded by

$$\frac{1}{Q_i} = \frac{1}{Q_{ph-ph}} + \frac{1}{Q_{TLS}} + \frac{1}{Q_{scatt}} + \frac{1}{Q_{therm}} \tag{2.56}$$

Geometrical loss: clamping

Another type of loss arises from the finite extent of the confining resonator surfaces. It can be estimated for a specific eigenmode of the finite resonator by looking at the ratio of its acoustic energy lying outside of the region which is encompassed by the HBAR dome to the total mode energy [17]

$$R = \frac{E_{out}}{E_{tot}} = \frac{\int_{out} |u|^2 dr}{\int_{tot} |u|^2 dr} \tag{2.57}$$

From this, one can compute a lower bound of the phonon lifetime for a resonator of thickness t assuming that all the energy lying outside of the encompassed region is lost.

$$\tau = -\frac{2t}{v_l} \frac{1}{\ln(1-R)} \tag{2.58}$$

This lifetime is associated with the quality factor

$$Q_{cl} = -2\pi f \tau = -\frac{4\pi t f}{v_l} \frac{1}{\ln(1-R)} \tag{2.59}$$

In the case of a paraxial Gaussian beam, the fundamental mode is of the form

$$u(x,y,z) = u_0 \exp\left(-\frac{x^2+y^2}{w_0^2}\right) \cos\left(\frac{m\pi x}{t}\right) \tag{2.60}$$

where w_0^2 is the beam waist. Then, the ratio R for a resonator with a dome of lateral extent d becomes

$$R = \exp\left(-\frac{d^2}{2w_0^2}\right) \tag{2.61}$$

Therefore, for the Gaussian beam one has the quality factor

$$Q_{cl} = -\frac{4\pi t f}{v_l} \frac{1}{\ln\left(1 - \exp\left(-\frac{d^2}{2w_0^2}\right)\right)} \tag{2.62}$$

An alternative method that is proposed to estimate the diffraction loss is by integrating the outward pointing mechanical power flux I_m, which gives the associated quality factor

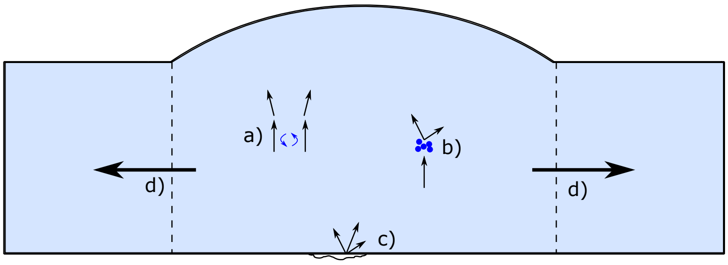

Figure 2.4: Main loss mechanisms in a HBAR: a) Phonon-phonon interaction, b) Impurity ions scattering, c) Surface scattering, d) Diffraction loss, which can be estimated by looking a the mode energy in the region under the dome versus the energy outside.

$$Q = \frac{E_{tot}}{\int_A d\vec{I}_m \cdot \vec{n}_r} \tag{2.63}$$

It is expected that diffraction loss increases with increasing radial mode index of Laguerre-Gaussian modes, as the energy of the modes becomes more spread out.

To summarize, a schematic of all described loss mechanisms is shown in Figure 2.4.

2.2.4 Electromechanical loss: Radiation

A particular loss present in cQAD systems stems from the interaction of the electric field of a qubit with phonons in some substrate by means of piezoelectricity. Just as atoms can emit photons when decaying because of coupling to the environment in spontaneous emission, the field of the qubit may decay into phonon modes. Quantitatively, this loss can be derived in the Weisskopf-Wigner theory for a Hamiltonian H_0 with a spectrum that has both discrete eigenstates

$$H_0|a_i\rangle = a_i|a_i\rangle \tag{2.64}$$

and a continuum

$$H_0|\epsilon\rangle = \epsilon|\epsilon\rangle \tag{2.65}$$

as is done in [31, 32]. Adding a perturbation or interaction term H_{int} may cause the discrete eigenstates to transition into the continuum, and the total Hamiltonian becomes

$$H = H_0 + H_{int} \tag{2.66}$$

The eigenstates of the total Hamiltonian are no longer $|a_i\rangle$ and $|\epsilon\rangle$. However, one can write the time evolution as their superposition

$$|\psi(t)\rangle = \sum_i \gamma_i(t)e^{-i\omega_i t}|a_i\rangle + \int_C d\epsilon \mathcal{D}(\epsilon)e^{-i\omega_\epsilon t}\gamma_\epsilon(t)|\epsilon\rangle \tag{2.67}$$

where ω_i and ω_ϵ denote the frequency of the eigenenergies, the integral is over the continuum C and the density of states at energy ϵ is denoted by $\mathcal{D}(\epsilon)$. In the special case where there is only a single discrete state, this simplifies to

$$|\psi(t)\rangle = \gamma_a(t)e^{-i\omega_a t}|a\rangle + \int_C d\epsilon \mathcal{D}(\epsilon)e^{-i\omega_\epsilon t}\gamma_\epsilon(t)|\epsilon\rangle \tag{2.68}$$

This time evolution can be inserted into the time-dependent Schrödinger equation

$$H|\psi\rangle = i\hbar\frac{\partial}{\partial t}|\psi\rangle \tag{2.69}$$

Multiplying from left with $\langle a_i|$ and $\langle\epsilon|$ yields the two equations

$$i\hbar\dot{\gamma}_a(t) = \int_C d\epsilon e^{i\Delta\omega t}\mathcal{D}(\epsilon)\gamma_\epsilon\langle a|H_{int}|\epsilon\rangle \tag{2.70}$$

$$i\hbar\dot{\gamma}_\epsilon(t) = e^{-i\Delta\omega t}\gamma_a\langle\epsilon|H_{int}|a\rangle \tag{2.71}$$

Equation 2.71 can be integrated formally and inserted into equation 2.70 to give

$$\dot{\gamma}_a(t) = \int_C d\epsilon e^{i\Delta\omega t}\mathcal{D}(\epsilon)\langle a|H_{int}|\epsilon\rangle \int_0^t dt' e^{-i\Delta\omega t'}\gamma_a(t')\langle\epsilon|H_{int}|a\rangle \tag{2.72}$$

It can be seen that $\dot{\gamma}_a$ depends on the integral of $\gamma_a(t')$ for all times up to t. An approximation to this is to set $\gamma_a(t') = \gamma_a(t)$, i.e. to make the markovian assumption, such that $\gamma_a(t')$ is independent of values at previous times. After performing the second integral in equation 2.72 and letting $t \to \infty$, one finds

$$\dot{\gamma}_a(t) = -\frac{2\pi}{\hbar}\mathcal{D}(\epsilon)|\langle a|H_{int}|\epsilon\rangle|^2\gamma_a(t) \tag{2.73}$$

whose solution gives the decay rate

$$\Gamma_a = \frac{2\pi}{\hbar}\mathcal{D}(\epsilon)|\langle a|H_{int}|\epsilon\rangle|^2 \tag{2.74}$$

We see that the decay is proportional to the density of states and the transition matrix element, which describes the coupling. However, one small comment has to be made about a particular assumption: in equation 2.68, the spectrum was assumed to have a single bound or discrete mode. As there might be coupling terms between discrete states, and we typically have several bound modes, this is has to be kept in mind.

This decay calculation can be applied to the case of a planar qubit separated by a piezoelectric layer to an infinite slab of substrate. As shown in Figure 2.5, the electric field of the qubit may couple to acoustic plane waves radiating away from the substrate. This situation is approximately the experimentally relevant case of a substrate slab of

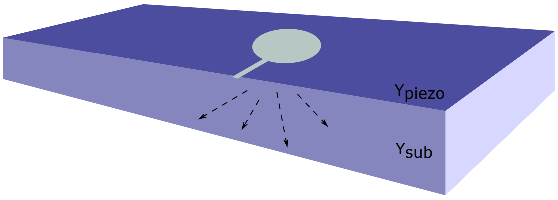

Figure 2.5: Representation of radiation loss of a qubit antenna (grey), whose electric field couples to phonons via the piezoelectric layer with Young's modulus Y_{piezo}, into a substrate slab with Y_{sub}.

finite thickness but with a large surface roughness on the face opposite to the piezo layer. For plane waves with longitudinal polarization $\hat{k} = \vec{k}/\|k\|$ in a substrate with Young's modulus Y_{sub}

$$\vec{s}_{\vec{k}}(\vec{x}) = \sqrt{\frac{\hbar\omega}{Y_{sub}V}}\hat{k}e^{-i\vec{k}\vec{x}} \tag{2.75}$$

where the prefactor is to normalize the states according to

$$\int \frac{1}{2}Y_{sub}|\vec{s}_{\vec{k}}|^2 dV = \frac{\hbar\omega}{2} \tag{2.76}$$

the coupling between the electric field and the acoustic plane waves can be computed as the overlap integral between induced strain $\vec{\sigma} = Y_{piezo}d\vec{E}$ from the qubit field, d being the piezoelectric tensor, and the strain plane wave, which becomes a function of the three dimensional Fourier transform of $\vec{A}(x) = d\vec{E} \cdot \hat{k}$

$$g_{\vec{k}} = \frac{1}{\hbar}\int dV\vec{\sigma} \cdot \vec{s} \tag{2.77}$$

$$= \frac{Y_{piezo}}{\hbar}\sqrt{\frac{\hbar\omega}{Y_{sub}V}}\mathcal{F}(A)(\vec{k}) \tag{2.78}$$

It has to be pointed out that the electric field of the qubit can be extracted from finite element method simulations. The coupling in k-space can then be used to estimate a decay to the continuum of phonon modes with the Weisskopf-Wigner theory. Assuming a density of states for countable energy levels, that is,

$$\mathcal{D}(\epsilon) = \sum_{\vec{k}} \delta(\epsilon_{\vec{k}} - \epsilon) = \frac{1}{\hbar}\sum_{\vec{k}} \delta(\omega_{\vec{k}} - \omega) \tag{2.79}$$

equation 2.74 becomes

$$\Gamma = 2\pi \sum_{\vec{k}} \left|g_{\vec{k}}\right|^2 \delta(\omega_{\vec{k}} - \omega) \tag{2.80}$$

$$= \frac{2\pi}{\hbar} \frac{Y_{piezo}^2 \omega}{Y_{sub}} \frac{1}{V} \sum_{\vec{k}} \mathcal{F}^2(A)(\vec{k}) \delta(\omega_{\vec{k}} - \omega) \tag{2.81}$$

$$= \frac{2\pi}{\hbar} \frac{Y_{piezo}^2 \omega}{Y_{sub}} \int dk^3 \mathcal{F}^2(A)(\vec{k}) \delta(\omega_{\vec{k}} - \omega) \tag{2.82}$$

$$\tag{2.83}$$

In the second step, the usual transformation of densities of states from a sum to an integral is used. The interpretation of the delta distribution ensuring energy conservation could read as follows: since the slowness surface of the substrate material in which the the plane waves radiate, is the surface of constant frequency, only wavevectors lying on this surface contribute to the decay at a given frequency.

A second concrete example is a substrate slab that has negligible surface roughness on the face opposite to the piezoelectric layer but is still infinite in the other two dimensions (choosing arbitrarily the vertical direction as z), such that only acoustic modes satisfying the discrete dispersion relation for the wavevector $k_{perp}^2 = k_x^2 + k_y^2$

$$\omega(k_\perp) = \sqrt{v_l^2 \left(\frac{n\pi}{t}\right)^2 + v_t^2 k_\perp^2}, n \in \mathbb{N} \tag{2.84}$$

can exist. The confinement expresses itself as the discretization of the wavevector in z-direction. The dispersion relation implicitly defines the density of states which is to be used in 2.84. In the approximation that the electric field of the qubit is mainly perpendicular to the piezo surface, which we define as the z-direction, such that we have $d\vec{E} \approx d_{33} E_z$, the coupling will have the form

$$g_k = s_0 c_{33} \frac{d_{33}}{\hbar k_0} \hat{E}_z(k) \tag{2.85}$$

that leads to the decay rate

$$\Gamma = 2\pi \int dk_\perp |g_k|^2 \mathcal{D}(\omega_q) \tag{2.86}$$

This means that under the assumptions taken, the Fourier transform of the electric field of the qubit can be shaped to minimize the coupling to the continuum of phonons and thereby also the decay rate. Finally, from the decay rate due to the coupling, one can extract the associated quality factor

$$Q = \frac{\omega}{\Gamma} \tag{2.87}$$

which can be compared to the other partial quality factors of the system.

2.3 Acoustic Schrödinger Equation

2.3.1 Motivation

In order to estimate the qubit decay rate due to phonon radiation, the density of phonon states in the HBAR and substrate are needed. The approach taken here is to use an acoustic analogy to the case of electromagnetic radiation propagation in the presence of a massive particle subject to the Schrödinger equation (SE) [33] called the "Optical Schrödinger Equation". One can use the solutions of such a Schrödinger equation to calculate the phononic density of states. In essence, for an optical cavity, the spatial variation of the refractive index can be translated to an effective potential in a modified SE. As a result, solutions of this equation describe the allowed bound and unbound states in the system.

In the optical case, a comparison is drawn to the electromagnetic wave equation in the monochromatic and paraxial approximation, which by a redefinition of the independent propagation variable takes the form of a non-relativistic SE of a massive particle in a 2D potential

$$i\hbar\frac{\partial}{\partial\tau}\psi(x,y;\tau) = -\frac{\hbar^2}{2m_{opt}}\nabla_\perp^2\psi(x,y;\tau) + V_{opt}(x,y;\tau)\psi(x,y;\tau) \tag{2.88}$$

where the optical mass is $m_{opt} = (\hbar k_0 n_0)^2$ and the optical potential can be expressed as a function of the spatial refractive index $n(\vec{r})$ and the vacuum refractive index n_0

$$V_{opt} = -\frac{1}{2}\left[\frac{n^2(\vec{r}) - n_0^2}{n_0^2}\right] \tag{2.89}$$

2.3.2 Derivation for acoustic waves

In the acoustic case, we start by looking at a non-isotropic solid with transverse velocities $v_x = v_y = v_t$ and a longitudinal velocity which depends on the refractive index n as

$$v_l(x,y) = \frac{v_0}{n(x,y)} \tag{2.90}$$

The wave equation for the displacement $\vec{u}$ can be written as

$$v_t^2(x,y)\nabla_\perp^2\vec{u} + v_l^2(x,y)\frac{\partial^2\vec{u}}{\partial z^2} - \frac{\partial^2\vec{u}}{\partial t^2} = 0 \tag{2.91}$$

where $\nabla_\perp = (\partial/\partial x, \partial/\partial y)$. We are interested in the case where the wave mainly propagates along the direction perpendicular to the cavity surfaces, which we take to be the z-direction. Hence, the ansatz of a monochromatic plane wave of frequency ω and wavevector k with slowly varying envelope $u_0(\vec{r},t)$ which is polarized in longitudinal direction

$$u_z(\vec{r},t) = u_0(\vec{r},t)e^{i(kz-\omega t)} \tag{2.92}$$

in used. Inserting it into the wave equation leads to

$$v_t^2\nabla_\perp^2 u_0(\vec{r},t) + v_l^2\frac{\partial^2 u_0(\vec{r},t)}{\partial z^2} + 2ikv_l^2\frac{\partial u_0(\vec{r},t)}{\partial z} - k^2v_l^2 u_0(\vec{r},t) + \omega^2 u_0(\vec{r},t) = 0 \tag{2.93}$$

Since $u_0(\vec{r},t)$ is varying slowly, the wave propagates mainly in the z direction. Therefore, one can make the paraxial approximation

$$\left|\frac{\partial^2 u}{\partial z^2}\right| \ll \left|k\frac{\partial u}{\partial z}\right| \tag{2.94}$$

where the angle between the wavevector and the propagation axis z is small. This justifies dropping the second term in Eq. 2.93 and dividing by $2k^2$ yields

$$\frac{i}{k}\frac{\partial u_0}{\partial z} = -\frac{1}{2k^2}\frac{v_t^2}{v_l^2}\nabla_\perp^2 u_0 + \frac{1}{2}(1-n^2(x,y))u_0 \tag{2.95}$$

Now, a change of variables to $\tau = kz$ is performed, which leads to

$$i\frac{\partial}{\partial\tau}u_0(x,y,\tau) = -\frac{1}{2k^2}\frac{v_t^2}{v_l^2}\nabla_\perp^2 u_0(x,y,\tau) + \frac{1}{2}(1-n^2)u_0(x,y,\tau) \tag{2.96}$$

Crucially, this now has the form of a time-dependent SE with $m = k^2$, $\hbar = 1$ and a potential $V = \frac{1}{2}(1-n^2(x,y))$. We can see that in the paraxial approximation, we can associate a spatially dependent refractive index to a potential term. To find an expression for this effective refractive index, one can use its relationship to the phase. For a resonator, the phase that is picked up in a round-trip is

$$\phi(x,y) = k(z_0 + m_2(x,y) - m_1(x,y)) = kn(x,y)z_0 \tag{2.97}$$

where m_1, m_2 denote the spatial profiles of the bounding surfaces of the resonator, as shown in Figure 2.6. Therefore, shaping the surfaces within the limits of the approximations used, one can engineer a desired spectrum, as will be described in more detail below.

Potential induced by a spherical dome

Taking the example of a finite spherical plano-convex cavity defined by its curvature R, height h and thickness z_0. Defining the radius of the dome raised above the substrate as $r_0 = \sqrt{2Rh}$, one has

$$m_1(x,y) = 0 \tag{2.98}$$

$$m_2(x,y) = \begin{cases} 0 & x^2+y^2 > r_0^2 \\ h(1-\frac{x^2+y^2}{r_0^2}) & x^2+y^2 \le r_0^2 \end{cases} \tag{2.99}$$

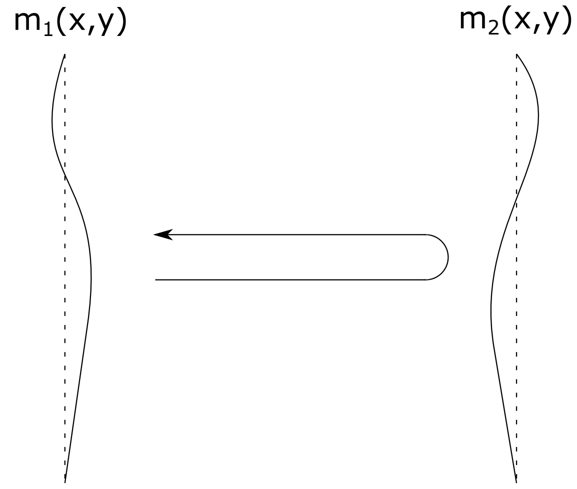

Figure 2.6: The difference in shape of the reflection boundaries m_1, m_2 of an acoustic resonator modulates the effective spatial refractive index in the acoustic Schrödinger equation, giving rise to a potential-like term.

This corresponds by equation 2.97 to the effective refractive index

$$n(x,y) = \begin{cases} 1 & x^2+y^2 > r_0^2 \\ 1 + \frac{h}{z_0}(1 - \frac{x^2+y^2}{r_0^2}) & x^2+y^2 \leq r_0^2 \end{cases} \tag{2.100}$$

Taking the square leaves

$$n^2(x,y) = \begin{cases} 1 & x^2+y^2 > r_0^2 \\ 1 + \frac{2h}{z_0}(1 - \frac{x^2+y^2}{r_0^2}) + \frac{h^2}{z_0^2}(1 - \frac{x^2+y^2}{r_0^2})^2 & x^2+y^2 \leq r_0^2 \end{cases} \tag{2.101}$$

The last term in the second case above can be dropped when $h \ll z_0$, which is the case for commonly fabricated domes with $h \approx 1\mu m$ on substrates with $z_0 \approx 400\mu m$. Hence, the final potential in the SE takes the form

$$V(x,y) = \begin{cases} 0 & x^2+y^2 > r_0^2 \\ \frac{h}{z_0}(\frac{x^2+y^2}{r_0^2} - 1) & x^2+y^2 \leq r_0^2 \end{cases} \tag{2.102}$$

Now that the time-dependent equation is fully determined, the plane wave ansatz

$$u_0(x,y,\tau) = e^{-i\eta\tau} u_\eta(x,y) \tag{2.103}$$

is inserted, such that the time-independent equation reads

$$\left(-\frac{1}{2k^2}\frac{V_t^2}{V_l^2}\nabla_\perp^2 + V(x,y)\right) u_\eta(x,y) = \eta u(x,y) \tag{2.104}$$

To get constructive interference and hence a stable mode, we require that the accumulated phase acquired in a round-trip is

$$2k(1-\eta)z_0 = 2\pi m, \quad m \in \mathbb{N} \tag{2.105}$$

We can now compare the acoustic equation to two-dimensional Schrödinger equation with a harmonic potential of stiffness $\kappa = \tilde{\omega}^2\mu$ for a mass μ, which in Cartesian coordinates reads

$$\left(-\frac{1}{2\mu}\nabla_\perp^2 + \frac{1}{2}\kappa(x^2+y^2)\right)\Psi = E\Psi \tag{2.106}$$

and can be solved for x and y independently, leading to the well-known eigenenergies

$$E_{xy} = E_x + E_y = \hbar\tilde{\omega}(n_x + n_y + 1) \tag{2.107}$$

with $n_x, n_y \in \mathbb{N}$ and degeneracy $D = n_x + n_y + 1$. The associated wavefunctions are products of the one dimensional harmonic oscillator solutions

$$\psi_n(x,y) = \psi_{n_x}(x)\psi_{n_y}(y) \tag{2.108}$$

The analogy to the acoustic Schrödinger equation can be completed by comparing Eqs. 2.104 and 2.106, such that one finds the equivalent to the effective mass μ and the spring constant κ of the harmonic oscillator to be

$$\mu \longleftrightarrow \left(\frac{kv_l}{v_t}\right)^2, \kappa \longleftrightarrow \frac{2h}{z_0 r_0^2} \tag{2.109}$$

in the case of the non-truncated acoustic potential. This allows one to estimate different quantities of interest for spherical domes, in particular for low energy states, as they are only weakly perturbed by the truncation. For example, the spacing between subsequent values of η is, according to Eq. 2.109,

$$\Delta\eta = \sqrt{\frac{2hv_t^2}{z_0 r_0^2 k^2 v_l^2}} \longleftrightarrow \tilde{\omega} = \sqrt{\frac{\kappa}{\mu}} \tag{2.110}$$

from which the "real" spacing in frequency can be computed by $\Delta\omega = \omega\Delta\eta$. The potential depth is $\frac{h\omega}{z_0}$ and the number of states with energies below zero (the bound states) is the potential depth divided by the frequency spacing

$$N = \left\lfloor \frac{h/z_0}{\Delta\eta} \right\rfloor \tag{2.111}$$

Another interesting quantity is the ratio of the depth of the potential to the longitudinal FSR, which is given by $\beta = \frac{mh}{z_0}$

$$FSR = \Delta\nu = \frac{c}{2L} \tag{2.112}$$

2.3.3 Application: shaping the spectrum

As mentioned above, the spectrum of the device as calculated with the acoustic Schrödinger equation leads to the interpretation that the surface shapes of the acoustic cavity themselves can be used to engineer the spectrum in a desirable way. For example, it was shown that spherical potentials lead to a harmonic potential approximately, and therefore to an even mode spacing throughout the bound part of the spectrum. This is in agreement with the even transverse mode spacing (TMS) of the Laguerre-Gaussian or Hermite-Gaussian mode family in plano-convex HBARs.

For quantum information protocols, this is not optimal, because the qubit may be required to not couple to any acoustic mode at certain times. Therefore, a frequency range within the FSR without a smaller density of modes is desirable and could be achieved with domes that deviate from the harmonic distribution. Small deviations could already make a difference, and because two examples that practically can be fabricated are Gaussian and cosine domes, these can be compared to spherical domes, which can be done by equating the Taylor expansions of the shapes parametrized by r up to second order. For the spherical dome of curvature R and height $h_{s,0}$ we have

$$h_s(r) = h_{s,0} - R + \sqrt{R^2 - r^2} = h_0 - \frac{r^2}{2R} + \mathcal{O}(r^4) \tag{2.113}$$

This can be compared to a cosine dome, whose height profile can be written as

$$h_c(r) = \frac{h_{c,0}}{2}\left[1 + cos\left(\frac{2\pi}{P}r\right)\right] = h_{c,0}\left(1 - \frac{\pi^2 r^2}{P^2}\right) + \mathcal{O}(r^4) \tag{2.114}$$

where the periodicity P can be used to match the spherical dome up to second order. This is achieved by setting

$$P = \pi\sqrt{2R} \tag{2.115}$$

Similarly, the Gaussian dome surface can be expanded as follows:

$$h_g(r) = h_{g,0}e^{-r^2/2\sigma^2} = h_{g,0}\left(1 - \frac{r^2}{2\sigma}\right) + \mathcal{O}(r^4) \tag{2.116}$$

Hence, if the heights are taken to be equal, we find the relation

$$\sigma^2 = R \tag{2.117}$$

These relations are used to compute the deviations from the harmonic spectrum in chapter 3. The resulting anharmonicity is quantified as

$$\alpha_i = \frac{(f_1 - f_0) - (f_i - f_{i-1})}{f_1 - f_0} \tag{2.118}$$

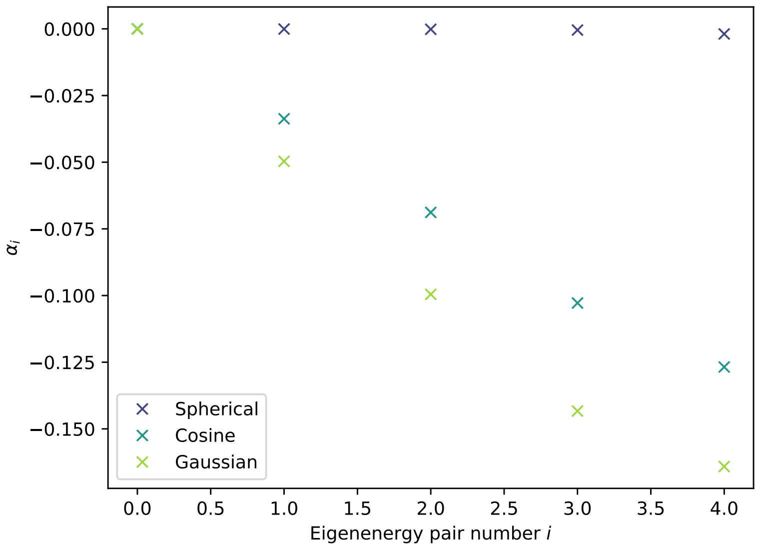

Figure 2.7: Computed anharmonicities from the ASE for the spherical baseline dome shape and equivalent cosine and Gaussian domes.

which can be easily computed from the solutions of the acoustic Schrödinger equation, the result being shown in Figure 2.7 for the three types of domes equivalent up to second order. This matches qualitatively the anharmonicities that are computed using a paraxial acoustic beam propagation method.

Chapter 3

Simulation Methods

In this chapter, the simulation methods that we used are described. For holistic modeling of the entire device consisting of a microwave cavity, a superconducting circuit and mechanical resonators, finite element method (FEM) simulations such as Ansys HFSS or COMSOL Multiphyics can be used to find classical field distributions, from which the quantum Hamiltonian and losses can be extracted according to the methods described in section 2.1. Typically, these simulations are conducted either in two or three dimensions. Although these methods promise the most accurate representation because they can include couplings of different physics present in real devices and have converging results for increasingly fine discretizations, the disadvantage of these methods lies in their high complexity, making it difficult to model the device and leading to long computation times compared to other methods. Moreover, the solutions suffer more from numerical errors, such that results are hard to interpret and may contain large amounts of artifacts. On the other hand, simpler methods for investigating the mode structure of HBARs are being developed, including Fourier propagation and a method based on the acoustic Schrödinger equation theory. Though these methods are less general, their results tend to be simpler to interpret.

3.1 COMSOL Multiphysics

COMSOL Multiphysics is a powerful FEM simulation environment that allows for the numerical simulation of many physical systems by solving the corresponding partial differential equations on desired geometries. Studies that can be conducted include time domain, frequency domain as well as eigenmode simulations, and in this work we focus on the latter two. Compared to other FEM methods, such as Ansys, COMSOL provides the flexibility to include arbitrary coupling terms between different types of physics, which is needed for a whole-device simulation of the $\hbar$BAR including both the electromagnetic fields in the microwave cavity and the acoustic waves in the substrate (in particular, in the HBAR). Although such simulations have been set up in [34], their complexity is such that many questions are still under investigation, and in this thesis, the methods used have been verified and extended.

3.1.1 General setup

COMSOL simulations are built according to a streamlined flow, requiring the user to define the information of the model in consecutive steps: variable definitions, geometry, materials, physics interfaces and finally the mesh. Once the model is built, the different simulation studies can be run.

Physics interfaces

In Physics interfaces the partial differential equations of the system to be solved, as well as constraints such as boundary conditions and loads, are defined. In our simulation studies, we use the physics interfaces *Solid Mechanics (sm)* and *Electromagnetic Waves, Frequency Domain (emw)* from the *Radio Frequency (RF)* module. The solid mechanics interface is part of the *Structural Mechanics* module of COMSOL. It solves the acoustic equations of motion together with a constitutive model of the solid material. As a result, displacements, stress and strains are computed. Here, a linear elastic material is used, which is described by the equations of motion presented in section 2.2.1. Because of the large amount of degrees of freedom that are needed to model the solid mechanics physics in substrates of sizes comparable to experimental devices, which become computationally infeasible even with the aid of high performance computing as provided by the ETH Euler cluster, only small regions of interest can solved with this interface. In particular, for the $\hbar$BAR device described in section 3.1.2, only in the region enclosed by the dome and the planar mirror surface solid mechanics are solved, whereas the substrate on which the qubit is placed is not simulated in solid mechanics. To emulate large substrates, low-reflecting boundaries are used, under the assumption that waves propagating away from the HBAR will be lost. The *emw* interface on the other hand solves Maxwell's equations in differential form together with the constitutive relations. Since these types of simulations have less degrees of freedom and the simulated geometry size is on the order of a wavelength, they can be solved throughout the entire microwave cavity.

To simulate superconducting objects, as for example the cavity and the qubit, a perfect electric conductor (PEC) boundary condition is set on the corresponding surfaces, whereas a perfect magnetic conductor (PMC) is used at the cross-section of the cavity to establish the symmetry such that only half of the cavity has to be simulated.

Materials

COMSOL provides a materials library which includes the needed material constants for every interface. This is convenient, since the cavity interior is modelled as vacuum, the substrates are Al_2O_3, and the piezoelectric dome consists of AlN, but the materials can be easily replaced.

Geometry

In the three dimensional case, all simulations where performed for a microwave cavity containing the $\hbar$BAR, cut in half to make use of the symmetry and hence reduce the number of degrees of freedom. The $\hbar$BAR is placed in the center of the cavity, and on its lower substrate, the qubit is drawn in two dimensions, neglecting its height. Since it has a disk attached to it via a transmission line, it is called *Antennamon.* Above the

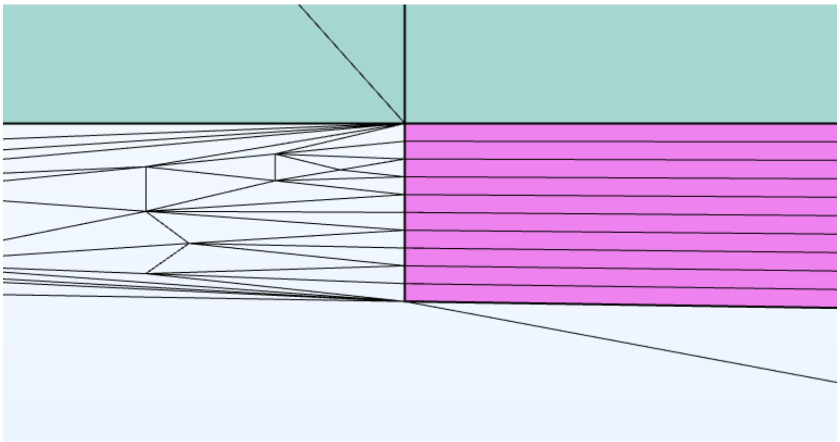

Figure 3.1: Example of degenerate mesh elements at the interface of the gap between the substrates (vacuum, white) and the dome edge (pink) attached to the top substrate (green), causing the meshing process to fail.

antenna, the HBAR consisting of the piezo-electric dome and the substrate is placed. A more detailed description will follow in section 3.1.3. On overview over the 3D model geometry can be seen in Figure 3.3. In the two dimensional case, only the HBAR was analyzed, defined by the revolution of a cross section of the HBAR.

Meshing

Meshing denotes the essential process in FEM by which the model geometry is discretized. The challenge in modeling cQAD devices such as the $\hbar$BAR comes from the large difference between electromagnetic and acoustic wavelengths under investigation. In general, it is recommended to set at least five mesh points per wavelength of the simulated physics, which leads to large size differences between the mesh elements in the vacuum of the cavity, where the microwave wavelength sets this limit, and the elements in the HBAR, where the wavelength of the acoustic waves are in the order of 1 μm. At some point, the element growth between these to regimes becomes bigger than the growth rate that COMSOL can handle, and the meshing process ends with an error. The large difference in element sizes leads to difficult transitions in the gap at the edges of the AlN dome, as shown in Figure 3.1.

Apart from these problems, the accuracy of the studies strongly depends on the actual form of the mesh elements. One important example is the radius of the cylinder inside the HBAR needed to mesh in a radially symmetric way. Although the frequency and mode waist of the simulated fundamental mode does not change with that radius, the resulting quality factors vary over a one order of magnitude, indicating that the quality factors computed by COMSOL are not yet fully physical. The results will be shown in chapter 4.

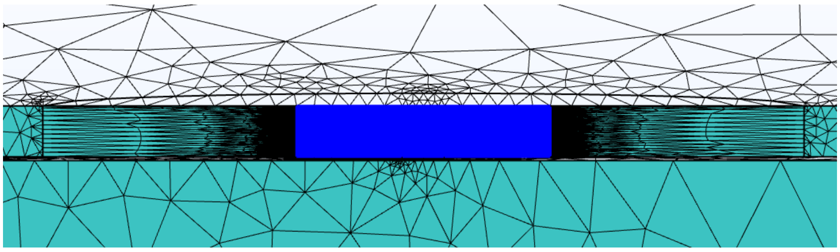

a Domain with high vertical mesh density in the region encompassed by the dome

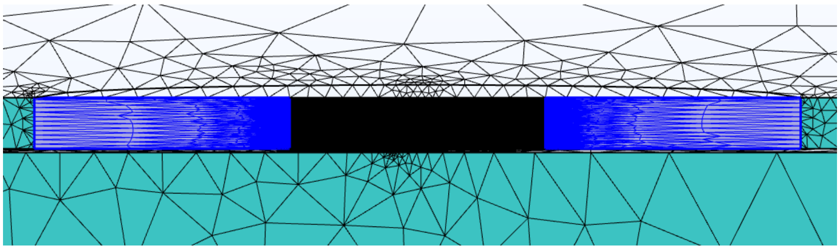

b Lateral virtual domain needed to adapt the high mesh density in the HBAR to the surrounding substrate.

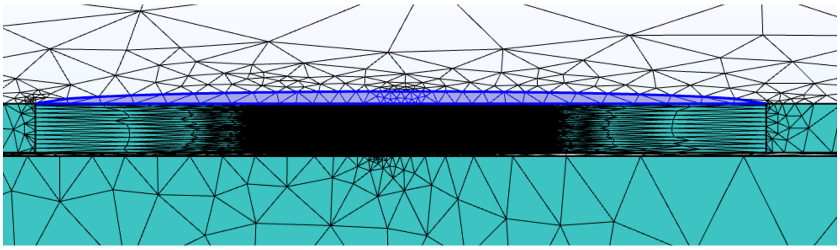

c Virtual domain used to transition to the relatively low mesh density in the vacuum of the cavity.

Figure 3.2: Cross sections of the HBAR model and its surroundings, depicting the mesh used in the baseline model. White elements correspond to the air domain, turquoise elements to sapphire substrates and the dark blue color highlights a specific domain.

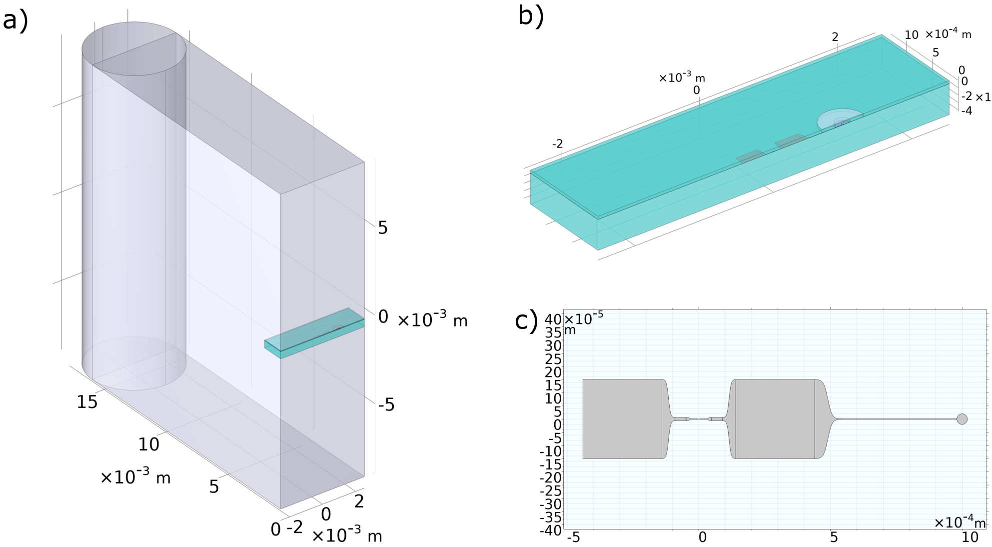

Figure 3.3: Geometry of the baseline model in COMSOL. a) The microwave cavity half simulated b) The $\hbar$BAR Substrate chip c) Antennamon qubit

Study types

In COMSOL, stationary, time dependent, eigenfrequency or frequency domain studies can be conducted. Here, only eigenfrequency and frequency domain are investigated. Furthermore, the studies can be uncoupled or coupled. In the first case, the device is simulated using solid mechanics and the *emw* physics interfaces separately. This functionality is provided by COMSOL "out of the box" but neglects the interaction between the electromagnetic field of the qubit and piezo materials, as mainly needed in the domes. On the other hand, this coupling can be manually implemented by making use of external sources for each of the two interfaces. In the case of the solid mechanics interface, the linear elastic material modelling the substrate is extended by an external stress by multiplying the electric field with the piezo-electric coupling tensor e in Voigt notation

$$\vec{S}_{ext} = -e^T \vec{E} \tag{3.1}$$

For the *emw* interface, the inverse piezo-electric effect is implemented by adding the external current density $\vec{J}_{ext}$ as a function of the strain T

$$\vec{J}_{ext} = i\omega e T \tag{3.2}$$

as a source term in the Helmholtz equation, which in the three dimensional case reads

$$\nabla \times (\mu_r^{-1} \nabla \times \vec{E}) - w^2 \epsilon_c \vec{E} = 0 \tag{3.3}$$

where μ_r and ϵ_c are the relative permeabilities and permittivities, respectively. Both frequency domain and eigenmode simulation studies can also be done in two dimensions. Since the HBAR is symmetric around a central axis, one can use axisymmetric simulations, which reduce the equation above to

$$\left(\nabla - i\frac{m}{r}\phi\right) \times \left(\mu_r^{-1}(\nabla - i\frac{m}{r}\phi\tilde{E})\right) - k_0^2\epsilon_{rc}\tilde{E} = 0 \tag{3.4}$$

where the independent variables are the radius r and azimuth angle ϕ, and the azimuthal mode number is m.

The computation time of a model depends strongly on the simulation type. It is stressed that frequency domain studies are computationally more expensive than eigenfrequency simulations. Also, simulating solid mechanics is more costly than the *emw* interface. Representative values of solution times can be seen in Table 3.1.

Study	Computation time
Eigenmode, SM only, 1 mode	3min
Eigenmode, SM only, 100 modes	30min
Eigenmode, EM only, 2 mode	3min
Eigenmode, Coupled, 10 modes	10min
Eigenmode, Coupled, 110 modes	9hrs
Frequency study, SM only, 1 FSR	18hrs
Frequency study, Coupled	not feasible

Table 3.1: Time needed to compute the COMSOL studies.

3.1.2 Devices to model

As already stated, COMSOL excels at modeling complex objects in which different physics are relevant. Therefore, it is used to investigate the hybrid quantum system used in this group consisting of a superconducting microwave cavity in which a transmon qubit with an antenna coupled to an HBAR, the $\hbar$BAR, is placed. The qubit and the HBAR are fabricated on separate sapphire substrate chips, which are bonded such that the centers of the antenna and HBAR match. The actual device is shown in Figure 3.4.

3.1.3 Baseline model

The model used as a baseline has a geometry similar to the experimental devices. The geometric parameters are shown in Table 3.2. The two main differences are the reduced thickness of the substrate (40 μm instead of 420 μm) to make the computations tractable and the dome shape, which has to include a small cylindrical layer at the interface to the substrate for meshing reasons. The material used for the substrate is Al_2O_3[i], while for the dome AlN was used. The qubit geometry is of an antennamon, a 3D transmon qubit with a disk (the antenna) attached to it. The dome shape is spherical. Because of

---

[i] Al_2O_3 is the main constituent of sapphire.

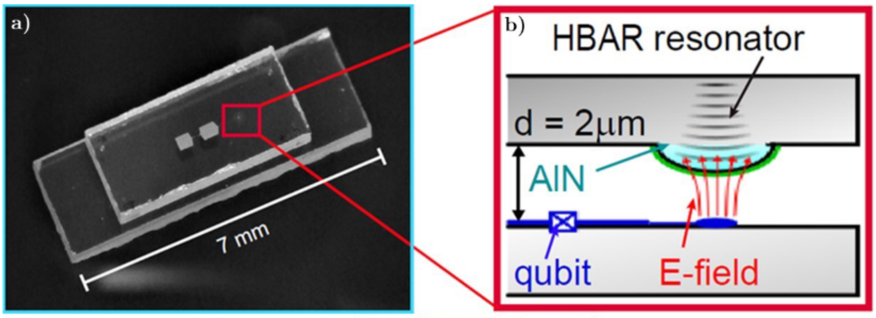

Figure 3.4: The $\hbar$BAR device modelled in COMSOL. a) The two bonded sapphire chips with the visible qubit pads and the dome (framed) of the HBAR b) Schematic of the coupling between the qubit and the HBAR (from [35])

inconsistencies, this model's accuracy was investigated thoroughly before proceeding to optimization.

Simulation domains

Ideally, both the differential equations of solid mechanics and electromagnetic waves would be simulated throughout the entire cavity. Although for the latter this is feasible and is in fact done in the baseline model, it is not possible to solve the solid mechanics physics in reasonable time on the entire top substrate (to which the dome is attached; the bottom substrate is not of interest because its mechanical modes are not coupled to the qubit), the reason for this is that the amount of degrees of freedom needed (see Table 3.3 for comparison) to resolve acoustic wavelengths in the micrometer range in a substrate of hundreds of micrometers is intractable. Therefore, solid mechanics is solved only in a small cylindrical region above the dome, because the eigenmodes of interest will be mainly paraxial and hence concentrated around the symmetry axis of the HBAR. A schematic depicting the region of the model around the HBAR is shown in Figure 3.5.

Meshing domains

To address the meshing challenges described above, the strategy used in the baseline model was to use a specific order in which different domains are meshed; first the HBAR and its surroundings, then the Josephson junction and finally the remaining domains are meshed. The order in which COMSOL meshes has an impact because generally the meshing process is constructive, that is, a subsequent mesh step does not modify the mesh from previous steps, although there are exceptional cases in which this does not hold. As explained, the solid mechanics domain consisting of the dome as well as a cylindrical cut above it, with the cylinder radius set to the transverse radius of the dome, is highly meshed. A *Swept Mesh* with a density of $8.825 \cdot 10^6$ m^{-1} along the z-direction is used. This type of meshing technique takes the mesh of a source face of the model and copies it at regular distances to a destination face. Between the copies, prismatic

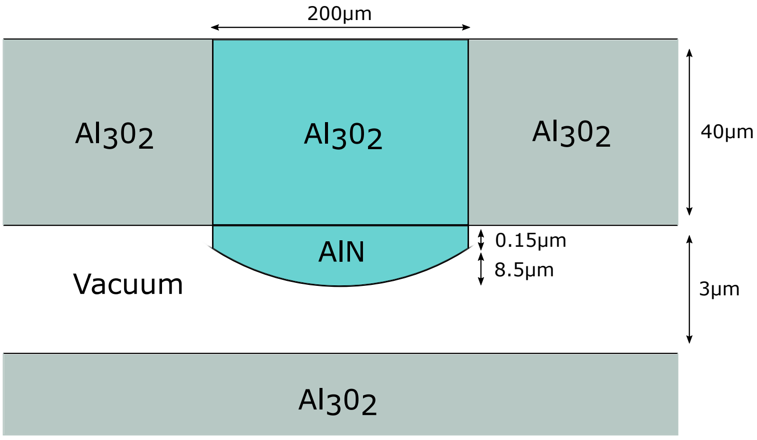

Figure 3.5: Materials and geometry of the HBAR of the baseline model, not to scale. Solid mechanics are only simulated in the turquoise region, electromagnetics in every domain. The radius of curvature of the dome is 7.14 mm.

or hexahedral mesh elements are created. The mentioned density used achieves the five elements per mechanical wavelength. Because of restrictions in COMSOL on how a mesh can be constructed, the dome has to be artificially offset from the substrate. This presents stringent constraints on how dense the mesh in the gap between the two substrates has to be. In particular, at the borders of the dome, where the mesh transitions from highly regular (swept) to tetrahedral elements, it becomes degenerate. This can be seen in Figure 3.1, showing how the angle between some mesh edges becomes small compared to the rest. To control the transition around the HBAR, virtual domains are used with an intermediate mesh density. Practical knobs include the amount of stretching of the mesh, as well as minimum and maximum element size and growth rate. The resulting mesh of the different meshing domains around the HBAR can be seen in Figure 3.2.

Parameter	Value
Cavity height	17.78 mm
Cavity width	5.08 mm
Cavity length	30.48 mm
Substrate height	40 μm
Radius r of HBAR	0.1 mm
Curvature R of HBAR	7.14 mm
Distance between antenna and pads	440 μm
Antenna radius	20 μm

Table 3.2: Main geometrical parameters of the microwave cavity, the HBAR and the qubit geometry, used in the baseline model.

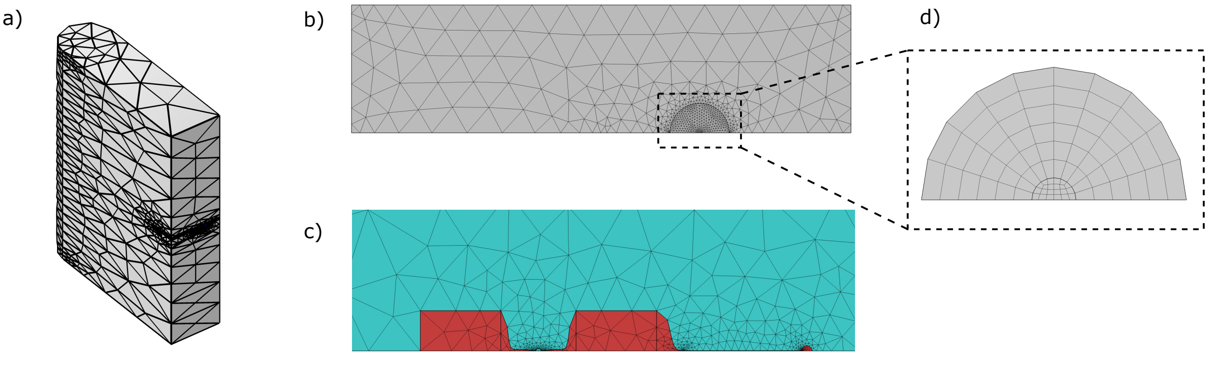

Figure 3.6: Finite element methods require a discretization of the simulation domain space, a procedure that is called meshing. The specific mesh strategy of the baseline model is shown for the a) microwave cavity, b) the substrate, c) the qubit (red) and d) dome.

Study	Degrees of freedom
SM only, 3D	778617 (+227304)
SM only 2D	45801
EM only 3D	1202538
EM only 2D	78013
Coupled	1981155 (+227304)

Table 3.3: Degrees of freedom for different types of studies for the baseline model. The numbers in brackets indicate additional internal degrees of freedom needed for solid mechanics.

3.1.4 Simulations in three dimensions

Uncoupled eigenmode simulations

In uncoupled eigenmode simulations, the electromagnetic waves and the solid mechanics interfaces are solved separately. In the former case, one finds the hybridized qubit-cavity eigenmodes, which are shown in Figure 3.7. Since higher order modes are at much higher frequency, they are not of interest in the following. In the latter case of uncoupled solid mechanics simulations, the eigenmodes of the HBAR displacement field and are expected to be Laguerre-Gaussian or Hermite-Gaussian modes. Indeed, for the spherical dome of the baseline model, the Hermite-Gaussian mode family is found, as can be seen in Figure 3.8.

A major challenge concerning COMSOL simulations of the HBAR is the interpretation of the resulting modes. A large fraction of the them have the following characteristics: they have displacement fields which appear noisy or random, have high spatial frequency

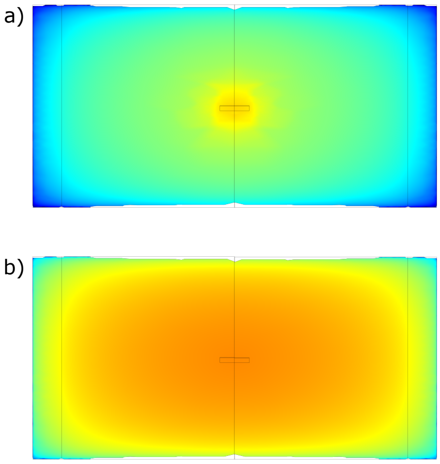

Figure 3.7: Logarithm of the electric field amplitudes of the uncoupled eigenmodes of the electric field in the microwave cavity. a) Qubit-like mode at 6.422GHz and b) Cavity-like mode at 9.1391GHz

components, and are large only at single points or at the cylindrical border region of the simulated solid mechanics. Therefore, the question arises whether these "spurious" modes represent physical solutions or not, and how to distinguish them. This is not trivial, as the analytical solutions for arbitrary geometries of the dome do not exist and the spurious modes can have a similar appearance as "real" ones. The distinction is important, as they may impact computations in further processing, for example in the EPR method. Problematic is also that the amount of solutions that look plausible is typically less than ten percent, creating a large computational overhead. Examples of spurious modes are shown in Figure 3.9.

Another interesting quantity to be extracted from uncoupled solid mechanics simulations is the diffraction loss of the HBAR modes, which will be shown in section 4.

Combining the electric fields and the mechanical modes from the uncoupled equations allows the computation of the approximate coupling rates of the system between the electromagnetic mode n and the mechanical mode m as [34]

$$\frac{g_{nm}}{2\pi} = \frac{\sqrt{\frac{\omega_n}{\omega_m \rho \epsilon_0}} \int_{V_p} \vec{E}_n^*(\vec{x}) e^T \varepsilon_m(\vec{x}) dV}{4\pi \sqrt{\int_V \vec{E}_n^*(\vec{x}) \epsilon_r \vec{E}_n(\vec{x}) dV} \sqrt{\int_V \vec{u}_m^*(\vec{x}) \vec{u}_m(\vec{x}) dV}} \tag{3.5}$$

Frequency domain simulations

In addition to eigenmode methods, we also implemented frequency domain studies in COMSOL. On one hand, this was done to verify the results of a simulation method previously used, and on the other, to assess whether it could be used for more complex resonator geometries. Compared to eigenmode simulations, one can also extract the

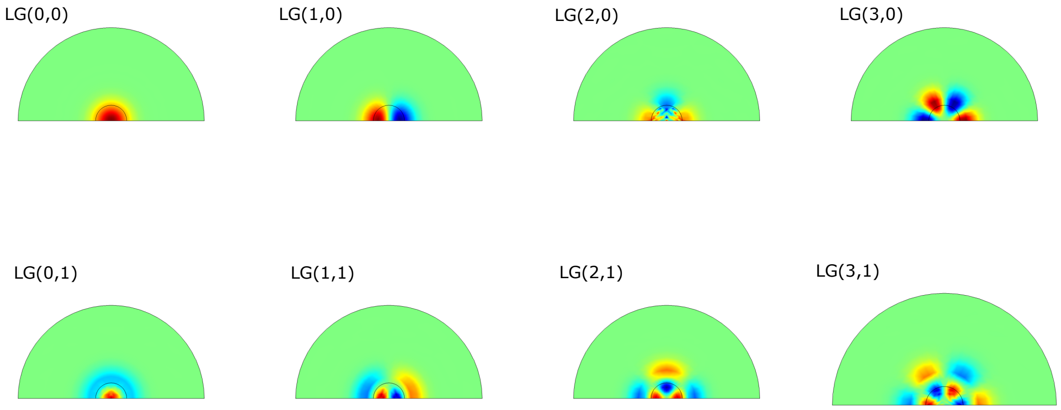

Figure 3.8: Lowest eigenmodes of a uncoupled solid mechanics simulation of the baseline model showing Laguerre-Gaussian LG(l,p) profiles.

linewidths of the resonances from the resulting spectra, providing a better understanding of the modes.

In order to implement a frequency domain simulation in COMSOL, boundary loads, which are time dependent boundary conditions, are added to the solid mechanics interface. The load direction and magnitude can be parametrized. For testing purposes, the driving function used is a Gaussian with amplitude A

$$\vec{f}_{drive}(x,y) = Ae^{\frac{-(x-x_0)^2-(y-y0)^2}{2\sigma^2}}e^{-i\omega t}\vec{e}_z \tag{3.6}$$

where x_0, y_0 denote the coordinates of the center of the HBAR and e_z is the unit vector in z-direction. Other types of forcing functions can be used as well. The load is applied as *Force per unit area* on the top (i.e. the flat) surface of the HBAR. After the driving function is defined, the frequency domain study node can be added and configured. Most importantly, the frequency range over which the study should be conducted has to be defined. For the HBAR which we investigated, which has only one-tenth of the thickness of the experimentally used substrate such that the FSR is in the order of 130 MHz, this sets a lower bound on the frequency span that should be simulated. A priori, it was not known whether the computations were feasible, so numerical experiments were conducted in two dimensions first, showing that for the given device geometry a frequency step size of 50 kHz resolved the resonances accurately in a reasonable computation time. The results of three types of domes are shown in Figure 3.10, where the spectra show the longitudinal displacements on the flat surface of the HBAR as a function of frequency.

We find a correspondence between the modes of the uncoupled eigenmode simulation and the centro-symmetric Laguerre-Gaussian modes on resonance in frequency domain

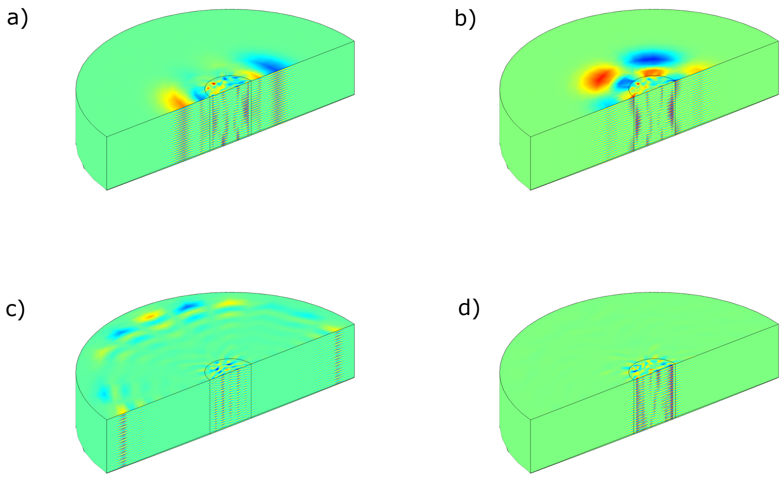

Figure 3.9: Examples of displacement fields, z component, of spurious modes in the results of uncoupled eigenmode solid mechanics simulations of the HBAR showing a) high spatial frequencies, b) large magnitudes, c) displacements concentrated on the border of the HBAR simulation domain d) displacements concentrated in the center region, meshed differently according to Figure 3.6.

simulation. We do not find other modes with higher radial index because the coupling between the centered Gaussian and those modes is zero due to symmetry.

It has to be noticed that these type of simulations are computationally very expensive, taking almost a day to solve a single FSR. Furthermore, the solution files require large amounts of memory, ranging to 40 Gb per FSR.

3.1.5 Simulations in two dimensions

As noted, 3D simulations are computationally costly. Therefore, to investigate the HBAR, 2D axisymmetric simulations were set up. As the name suggests, axisymmetric simulations can be used when the geometry of the object to model does not vary around a symmetry axis. Since this is the case for most domes, these simulations are appropriate for investigating mechanical modes in the HBAR. The only additional parameter to be set is the azimuthal mode number. The results of the two dimensional eigenmode simulations can be seen in Figure 3.11. In Figure 3.12 cross sections of the first three modes are shown. One can see that higher order modes couple significantly less to the Gaussian drive.

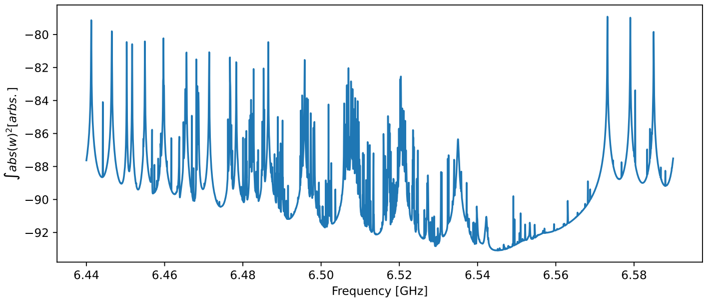

a Spectrum of the HBAR with spherical dome used in the baseline model.

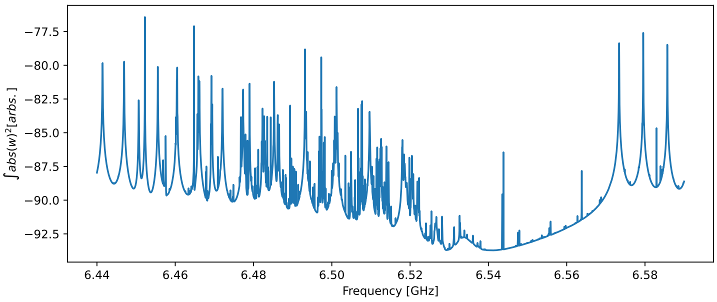

b Spectrum using a Gaussian dome.

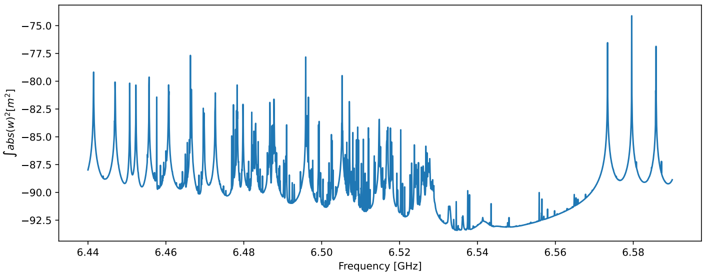

c Spectrum of a cosine dome.

Figure 3.10: Spectra over an FSR of the baseline model and two equivalent dome shapes. The fundamental modes are at 6.44 GHz and 6.57 GHz. Only small differences can be seen, but the spectrum of the cosine dome shows less modes at the end of the FSR and could be promising for applications needing mode-free frequency space.

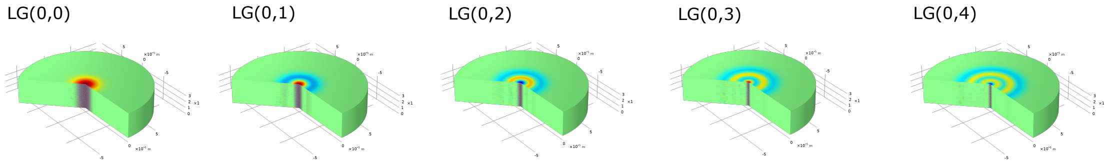

Figure 3.11: First five Laguerre-Gaussian modes LG(l,p) with azimuthal index l and radial index p for an HBAR with geometry as in the baseline model resulting from a 2D axisymmetric simulation.

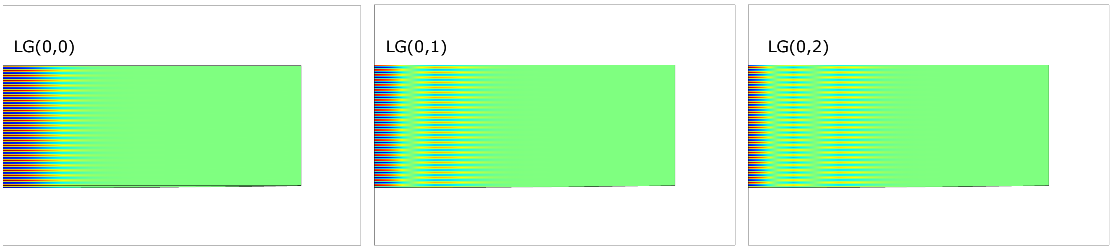

Figure 3.12: Cross cuts of the displacement field amplitudes in z direction from 2D eigenmode simulations of the HBAR corresponding to the revolution views shown in Figure 3.11. The bounding rectangles represent the simulation domain edges.

3.2 Fourier-propagation: BeamProp

Similar to optical Fourier methods in the paraxial limit, acoustic waves can be propagated in Fourier-space by simple multiplication of a phase. A description of the theoretical framework can be found in [36]. BeamProp is a python-based simulation library that implements the paraxial acoustic wave propagation in a HBAR resonator. It is used to compute the spectrum and corresponding eigenmodes resulting from a harmonic driving force. The implemented algorithm starts by preparing the surface profiles of both sides of the resonator (discretized on a two-dimensional grid), interpolates the slowness surface of the used material to get effective transverse and longitudinal velocities as described in section 2.2.1 and sets a driving force function $g(x, y)$, typically a centered Gaussian. This latter is used as an initial displacement field u_0. Also, for a given frequency, $k_z(k_x, k_y)$ is computed.

The paraxial propagation is repeated for many round-trips. For every round-trip, the displacement field at $z = 0$ is multiplied by the driving function $g(x, y)$, fourier-transformed and propagated along the positive z-axis as

$$u_{i,0}(x, y) = \mathcal{F}^{-1}(e^{-ik_z z}\mathcal{F}(gu_{i-1})) \tag{3.7}$$

Then, to account for the shape of the dome, the phase $\delta\phi_1$ that is picked up by the wave during propagation in the dome is computed according to an effective dome height. A reflection profile $R_1(x, y)$ accounts for internal losses and a damping at the boundaries of the simulation domain. Therefore, after reflection, the field at $z = L$ is

$$u_{i,1}(x, y) = R_1(x, y)e^{-i\delta\phi_1}u_{i,0}(x, y) \tag{3.8}$$

The field is transformed to Fourier space and propagated back to $z = 0$

$$u_{i,2}(x, y) = \mathcal{F}^{-1}(e^{-ik_z z}\mathcal{F}(u_{i,1})) \tag{3.9}$$

After adding the phase shift due to the second surface and the losses

$$u_{i,3}(x, y) = R_2(x, y)e^{-i\delta\phi_2}u_{i,2}(x, y) \tag{3.10}$$

a single round-trip is concluded and the propagated field is added to the total field,

$$u_i = u_{i-1} + u_{i,2} \tag{3.11}$$

which is then used as the initial field in the next round, leading to destructive interference for modes not supported by the resonator. The process is repeated for a range of frequencies, and the result is a spectrum of the displacement field amplitudes. In a second step, the mode profiles corresponding to the resonances in this spectrum can be extracted and refined by using computing more round-trips at these specific frequencies. This can provide an insight into the mode structure of the resonator, and also allow the computation of coupling rates. Furthermore, since this type of simulation has been used before, its results were compared to the newly implemented COMSOL frequency domain studies. The results are presented in chapter 4.

3.3 Acoustic Schrödinger Equation

3.3.1 Computational considerations

There are several ways to solve the ASE from section 2.3 numerically, namely as an eigenvalue problem, by means of numerical integration or using a finite element method. In the first case, the differential operator in equation 2.104 has to be discretized and written in matrix form. For two dimensional problems, this matrix grows quickly, making the computations expensive. In the second case, the differential equation can be integrated for the one dimensional case with standard tools, but numerical stability plays a key role. Furthermore, extending this method to two dimensions is not trivial. In the last case, the wavefunction is written as a linear combination of some basis functions defined on a regular mesh. In the following, we focus on the first two methods.

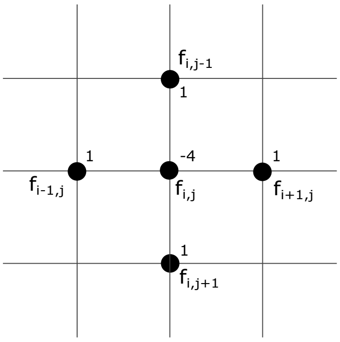

Figure 3.13: Five-point stencil typically used to discretized a 2D Laplacian operator as present in the Schrödinger equation. The corresponding matrix is therefore tri-diagonal.

Solution using eigendecomposition

To solve equation 2.106 by finding numerically its eigenvalues and functions, the equation has to be formulated in matrix form. For this, the operators have to be discretized. In the two-dimensional case the eigenvalue problem results in a sparse, tri-diagonal problem

$$-\frac{1}{2k^2}\frac{v_t^2}{v_l^2}\begin{bmatrix} a_{11} & a_{12} & 0\cdots & 0 \\ a_{21} & a_{22} & a_{23}\cdots & 0 \\ 0 & a_{32} & a_{33}\cdots & 0 \\ \vdots & \vdots & \vdots\ddots & \vdots \\ 0 & 0 & 0\cdots & a_{mn} \end{bmatrix}\begin{bmatrix} u_{x_0,y_0} \\ u_{x_0,y_1} \\ \vdots \\ u_{x_n,y_m} \end{bmatrix} + \begin{bmatrix} V_{11} & 0 & 0\cdots & 0 \\ 0 & V_{22} & 0\cdots & 0 \\ 0 & 0 & V_{33}\cdots & 0 \\ \vdots & \vdots & \vdots\ddots & \vdots \\ 0 & 0 & 0\cdots & a_{mn} \end{bmatrix}\begin{bmatrix} u_{x_0,y_0} \\ u_{x_0,y_1} \\ \vdots \\ u_{x_n,y_m} \end{bmatrix}$$

$$= \eta\begin{bmatrix} u_{x_0,y_0} \\ u_{x_0,y_1} \\ \vdots \\ u_{x_n,y_m} \end{bmatrix}$$

with size $nm \times nm$, where n are the number of mesh points in x, m the number of mesh points in y and the Laplace operator is discretized using a 5-point stencil finite difference method. To get an intuition for the discretization, away from the boundaries, the operator takes the form

$$\Delta f(x,y) \approx \frac{u_{i-1,j}, u_{i+1,j} + u_{i,j-1} + u_{i,j+1} - 4u_{i,j}}{\Delta x \Delta y} \tag{3.12}$$

the coefficients of which are visualized as in Figure 3.13. However, a more careful analysis is based on the discrete Taylor expansion of the function, which in the 1D case reads

$$f_{k+j} = \sum_{\alpha=0}^{\infty} \frac{1}{\alpha!}(j\Delta x)^\alpha f_k^\alpha \tag{3.13}$$

with Δx being the distance between two adjacent sampling points. The n-th derivative can then be written as a linear combination of function values around point x_k

$$\left(\frac{d^n f}{dx^n}\right)_k \approx \sum_{j \in A} c_j f_{k+j} \tag{3.14}$$

Here, A denotes the set of indices in the neighborhood of mesh point k,

$$A = -p, -p+1, ...k-1, k, k+1, ..., q-1, q \tag{3.15}$$

For example, in the case of $p = 1, q = 1$, the five-point stencil from equation 3.12 is recovered.

The algorithm is implemented in the Python package *FinDiff* [37], allowing the user to choose the accuracy in terms of number of points in A. At the boundaries of the domain, this also introduces modifications from equation 3.12, such that the Hamiltonian becomes non-hermitian in the approximation treated here and is therefore not exactly physical. Furthermore, standard algorithms for hermitian matrices can't be applied, increasing the computation time.

In general, the complexity of computing the eigenvalues of a matrix of size k scales as $\mathcal{O}(k^3)$, making it expensive to compute the solutions of the ASE on large two-dimensional configuration spaces compared to the one dimensional case. The reason for this is that the differential (Laplace) operator dimension scales with the product $N = mn$. To make an estimation of the time needed to solve, the equation was solved for different sizes of the Hamiltonian. This agrees with the aforementioned scaling. Furthermore, the accuracy of the eigenvalues for a given dome potential was investigated as a function of mesh points. The results of these investigations is shown in Figure 3.14. They indicate that the eigenfrequencies converge and that using more than 1.25 points per micrometer of substrate on a dome inducing a potential depth of about 25 MHz should be enough to resolve the energies accurately. However, these mesh densities lead to computation times in the order of few hours for two dimensional problems. Some tricks can be played on the solver configuration and the mesh (i.e., the use of non-uniform meshes, which are dense in regions where the potential in the Hamiltonian has a large curvature, and sparse in the regions where the potential is constant), but essentially the scaling of $\mathcal{O}(k^3)$ remains.

It should be noted further that for the relevant case of a harmonic potential, the eigenfrequencies of the two dimensional problem are degenerate and correspond exactly to the one dimensional solutions. Hence, for a truncated potential, one can approximately solve the one dimensional problem and predict the solutions in two. That this is reasonable in the parameter regime of fabricated domes, is shown in Figure 3.15. Further simulations were conducted, as for example the evaluation of the width of the substrate to be used, to see how big the impact on the eigenfrequencies might be. The results shown in Figure 3.16 show that the for a reasonable width between 400 μm and 1800 μm, the eigenfrequencies are almost unchanged. Furthermore, one can nicely observe the kink induced by the change of the potential width at the interface between the piezo and the sapphire dome, since the simulation was based on the Hero sample as used in [35]. The

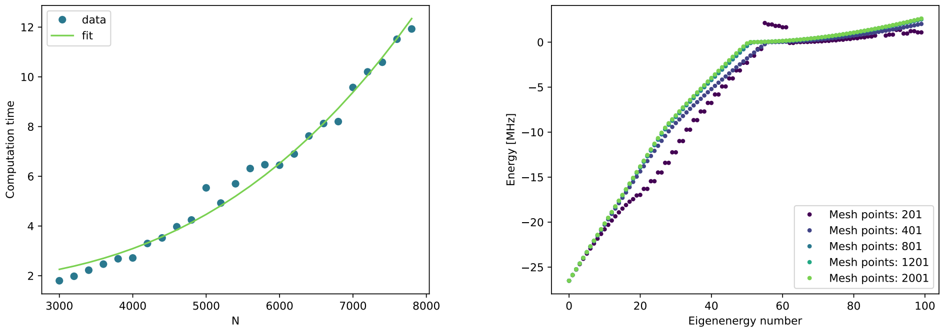

a b

Figure 3.14: a) Computation time needed to solve the ASE on a Intel i7-10700K processor at 3.80 GHz as a function of the corresponding Hamiltonian of size $N \times N$ scaling as $\mathcal{O}(N^3)$ b) Eigenfrequencies for different number of mesh points on a 800 μm substrate. Convergence happens after roughly 1000 points.

same simulation was done in the two-dimensional case, as shown in Figure 3.17. Here, the differences in the eigenfrequencies between different substrate sizes become more pronounced, in particular close to the edge of the potential well, there is an increasing frequency shift for those higher levels. One has therefore to be more careful with the results from 2D simulations.

Solution by numerical integration

An alternative approach for solving the acoustic Schrödinger equation in the 1D case consists of standard numerical integration. In this case, starting from an initial wavefunction and a trial energy, equation 2.106 is integrated. This is done for different energies until the wavefunction does not diverge anymore, which happens at the eigenenergy of the equation. More systematically, if an energy interval is given in which the eigenenergy is certainly found, a root-finding algorithm such as Brent's method can be used to find a wavefunction fulfilling

$$lim_{r\rightarrow 0}\Psi(r) = 0 \tag{3.16}$$

However, this method showed to have many disadvantages: first, an initial good guess for the energy range in which the eigenenergy should be found is not always given. Second, the integration method itself can diverge under certain circumstances. Third, the accuracy of the wavefunction solutions was not shown to be higher compared to the previous method.

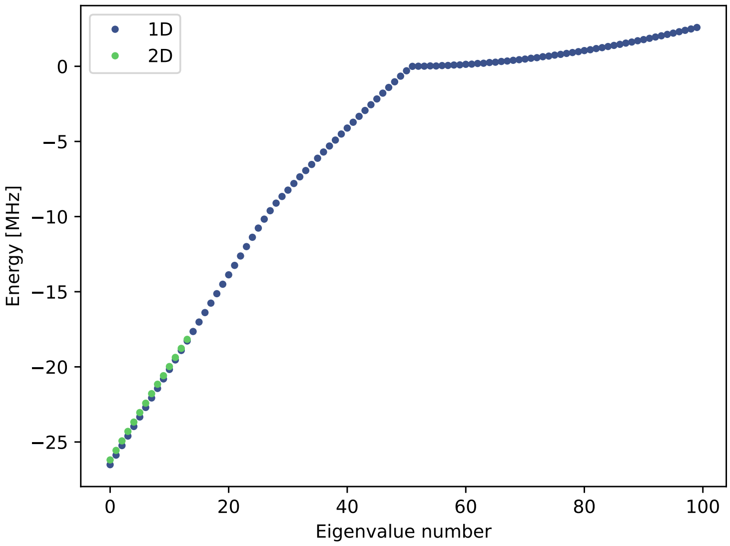

Figure 3.15: Comparison of the energy eigenstates in the Hero sample as in [35] for simulations in one and two dimensions. As expected, they agree well but not perfectly since for a harmonic oscillator the spectrum is the same in both cases except for degeneracy, but here the potential is capped. Only the lowest energy levels of the 2D simulation where computed, as they already take several hours of computation, and their degeneracies is not shown.

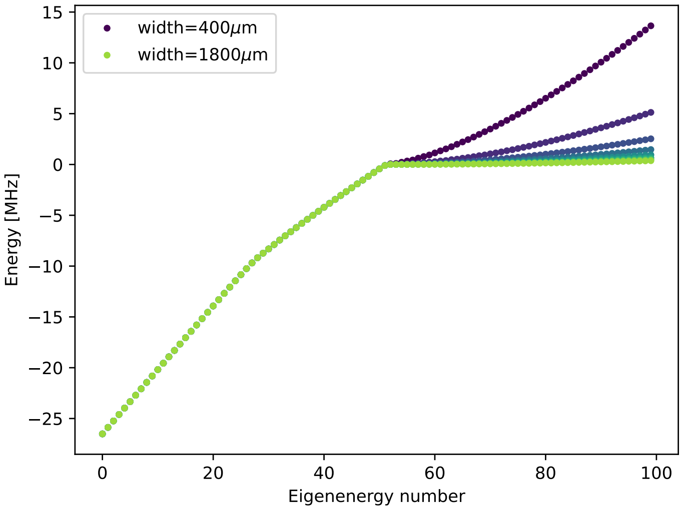

Figure 3.16: Numerical experiment with different sizes of substrate shows the emergence of a continuum of unbound states for widths increasing from 400 μm to 1800 μm for a dome with dimensions as in [35].

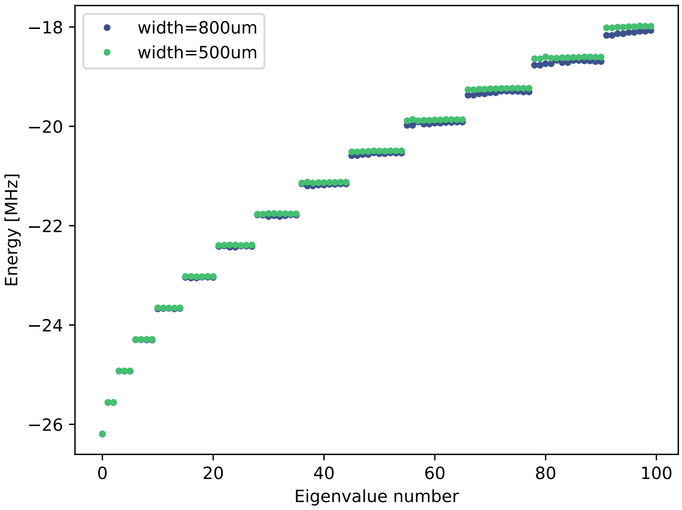

Figure 3.17: Impact of the simulated width of the substrate around the dome on the eigenenergies in the two dimensional case.

Radial Schrödinger equation

As explained above, solving the ASE on a two dimensional domain using the eigendecomposition method is computationally expensive. One interesting solution to this problem that was investigated is to solve the problem by making use of the radial symmetry of the dome shapes and hence potentials, in the approximation that the substrates dimensions are much bigger than the . Therefore, it seems more appropriate so solve the problem in a polar coordinate system. As a proof of principle that this method could be of use, it was investigated in atomic units ($e = m = \hbar = 1$). Therewith, the polar Schrödinger equation for azimuthal angle ϕ and radial coordinate ρ is [38]

$$-\frac{1}{2}\left(\frac{1}{\rho}\frac{\partial}{\partial\rho}(\rho\frac{\partial}{\partial\rho}+\frac{1}{\rho^2}\frac{\partial^2}{\partial\phi^2})\right)\psi=(E-V(\rho))\psi \tag{3.17}$$

As usual, a separation ansatz can be used

$$\psi(\rho,\phi)=R(\rho)\Phi(\phi) \tag{3.18}$$

which results in an equation for $\Phi(\phi)$ and $R(\rho)$ each. The first equation reads

$$\frac{\partial^2\Phi(\phi)}{\partial\phi^2}=-m^2, m\in\mathbb{N} \tag{3.19}$$

with the simple solution

$$\Phi(\phi)=e^{im\phi} \tag{3.20}$$

The radial equation, on the other hand, is given by

$$\rho^2\left(\frac{\partial^2 R}{\partial\rho^2}\right)+\rho\left(\frac{\partial R}{\partial\rho}\right)+(\rho^2k^2-m^2)R=0 \tag{3.21}$$

with $k^2 = 2(E - V(\rho))$, which can be rewritten to

$$\left[\left(\frac{\partial^2}{\partial\rho^2}\right)+\frac{1}{\rho}\left(\frac{\partial}{\partial\rho}\right)-\frac{m^2}{\rho^2}-2V(\rho)\right]R(\rho)=2ER(\rho) \tag{3.22}$$

The equation has the form of the known Bessel's equation, and for an infinite potential at $\rho = R_0$, that is

$$V(\rho,\phi)=\begin{cases}0 & \rho<R_0\\ \infty & \rho>=R_0\end{cases} \tag{3.23}$$

the solutions are indeed Bessel functions $J_m(k\rho)$, where the boundary condition $R(R_0)) = 0$ forces the wavevector to be quantized as

$$k_{ml}=q_{ml}/R_0 \tag{3.24}$$

Here, q_{ml} is the l-th root of $J_m(x)$ such that the wavefunction is zero at the infinite potential wall.

Hence, the two dimensional problem is reduced to one dimension for axisymmetric potentials, making the solution much faster. In the case of the ASE, the goal is to solve Bessel's equation with the radial potential induced by the shape of the resonator surfaces, with the boundary condition of the wavefunction going to zero for a large value of r. To solve the radial equation, we have again the possibility of using the eigendecomposition of the differential operator on the left, or by integration. For the former, the only difference to Cartesian coordinates is the appearance of the inverse of the independent variable ρ in the equation itself. This can be discretized into the diagonal matrix

$$\begin{bmatrix} 1/\rho_0 & 0 & 0\cdots & 0 \\ 0 & 1/\rho_1 & 0\cdots & 0 \\ 0 & 0 & 1/\rho_2\cdots & 0 \\ \vdots & \vdots & \vdots\ddots & \vdots \\ 0 & 0 & 0\cdots & 1/\rho_N \end{bmatrix} \tag{3.25}$$

where N denotes the number of discretization points in radial direction. Because the problem is reduced to finding the eigendecomposition of a matrix of size $N \times N$, the computation time of the problem is drastically reduced.

In the case of numerical integration of the radial equation, another concern comes into play: the direction of integration has typically to be chosen as starting from infinity (practically, this is implemented as starting at a large distance from the center $\rho = \rho_{max}$ and flipping the integration axis), instead of integrating from the origin, as otherwise the problem is not stable. Furthermore, the discretization is chosen to be logarithmically, instead of linear, because this improves stability for radial problems.

The method was tested with a harmonic potential and atomic units. The four lowest energy wavefunctions with $m = 0$ are plotted in Figure 3.18.

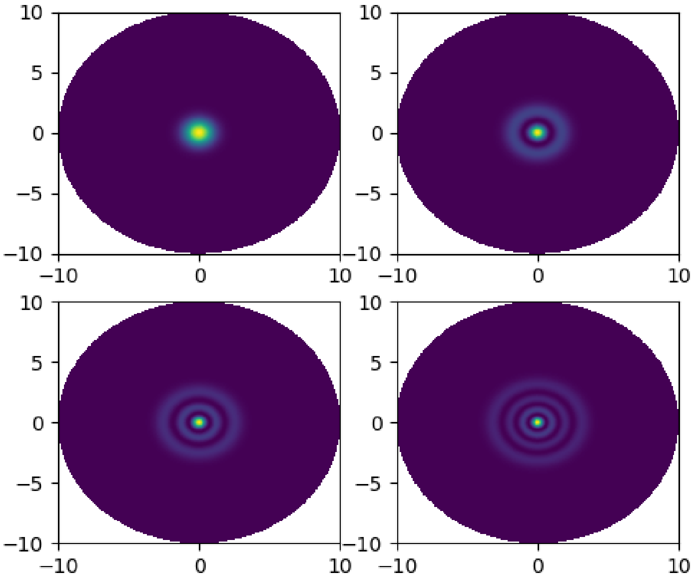

Figure 3.18: Wavefunction solutions of the two dimensional harmonic potential for the azimuthal order $m = 0$ using the radial Schrödinger equation in atomic units.

CHAPTER 4

Results

4.1 COMSOL simulations evaluation and consistency

One main result of this thesis is the evaluation and improvement of the accuracy of the existing COMSOL simulations of the hybrid quantum system $\hbar$BAR, as well as their extension to the frequency domain. In the following, the sensitivity of the results to the mesh (the discretization of the model in space) is presented, which is one important computational modeling freedom in any finite element method simulation tool such as COMSOL.

4.1.1 Longitudinal HBAR mesh

To investigate the accuracy of the solid mechanics simulations inside the HBAR, a study was conducted by varying the amount of mesh points along the z-direction in the domain in which solid mechanics are solved. The results of this study are shown in Figure 4.1.

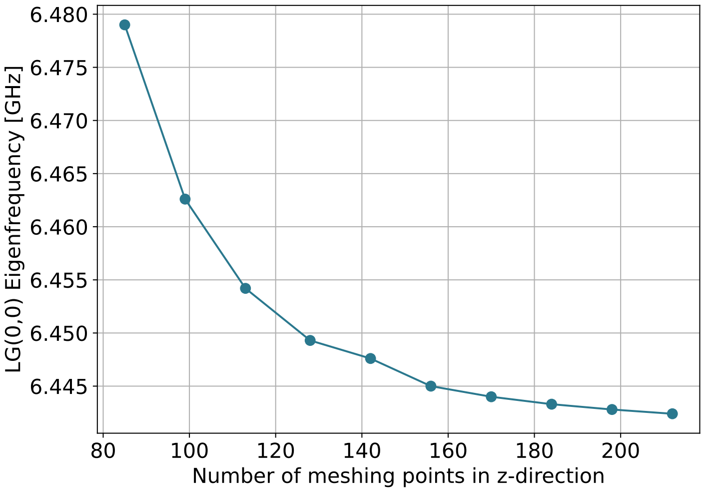

Figure 4.1: Mesh density study varying the number of mesh points in z-direction inside the HBAR showing a convergence of the fundamental mode eigenfrequency in an eigenmode simulation (with substrate length 40 μm).

They clearly indicate a convergence of the simulation results, and that for predictions of eigenfrequencies in the order of one megahertz in a device with a FSR in the order of 130 MHz, using a mesh density of more than 5×10^6 m^{-1} (which corresponds to 200 mesh points) is required. The reason for the decrease in eigenfrequency when increasing the number of mesh points can be explained by the computational stiffness stemming from the mesh, which increases with decreasing mesh density. This observation agrees with the fact that the FSR converges similarly to the eigenfrequencies.

4.1.2 Transverse HBAR mesh

The transverse mesh, defined on the top plane of the HBAR, has a large impact on the eigenmode solutions. As explained above, it consists of a center region of quadrilaterals, and an outer region, where the mesh is created by radially outgoing planes intersected by concentric cylinders. Experiments with the radius of the inner region show that the eigenmode displacement fields are consistent for radii between 0.1 μm and 0.4 μm. Larger radii can not be compared directly because the mesh that is generated becomes asymmetric. Once this happens, much more artifacts in the eigenmodes appear, which can corrupt the physical eigenmodes and even make them not appear in the results. Also, it should be noted that the quality factors computed by COMSOL, which are defined in the reference manual for an eigenvalue λ as

$$Q_{COMSOL} = \frac{\omega}{2|\mathrm{Re}\{\lambda\}|} \tag{4.1}$$

vary strongly with the radius of this mesh domain, and are possibly maximized when a mesh edge is at the beam waist of the mode, which indicates that the quality factor that COMSOL computes is mesh-dependent. On the other hand, the eigenfrequency of the modes are robust to the changes of the transverse mesh, which implies that the variation in the quality factors must be due to the computed eigenvalues. Because this value may be used in further calculations, this needs to be further investigated, for example by drastically increasing the transverse mesh density in the outer region of the solid mechanics domain. It can be concluded that it is not recommended to use the quality factor computed by COMSOL for the HBAR before this further sensitivity analysis has been done.

4.1.3 Qubit mesh

The mesh around the Josephson junction was varied to quantify how sensitive the results of the eigenmode simulations are regarding small model features, because the modelled junction has an area of 0.1×10^{-12} m^2 compared to the cavity dimensions of several centimeters. This was done by applying maximum mesh element size constraints in the junction. The results of electromagnetic eigenmode simulations of the baseline model with these variations are shown in Table 4.1, which demonstrates that eigenfrequencies are accurate to the level of tens of MHz for the baseline model. It is also interesting to look at the sensitivity of a measure of directionality of the electric field at the antenna

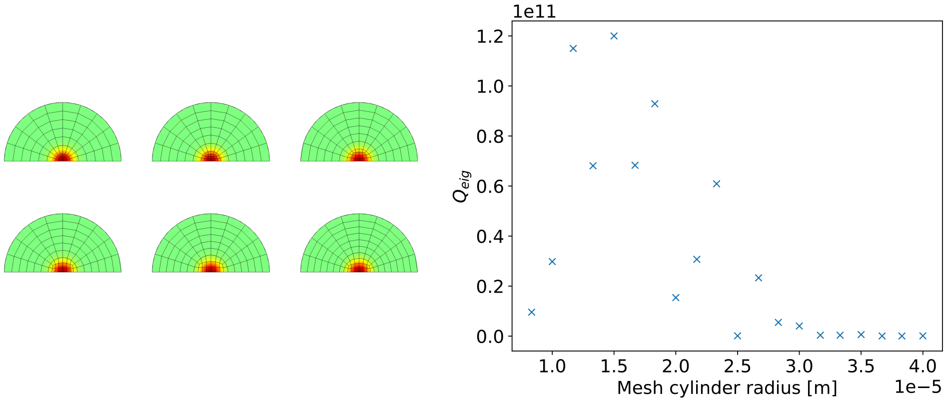

Figure 4.2: a) Displacement field on the top surface of the simulated solid mechanics domain. The fundamental eigenmodes are shown with increasing radii of the center mesh domain. The extracted beam waist of the mode profile at the flat surface of the HBAR is 1.24×10^{-5} m. b) Quality factors computed by COMSOL of one fundamental eigenmode of the HBAR at a frequency of 6.4412 GHz showing the impact of the transverse meshing using a longitudinal mesh density of 8.825×10^{6} m^{-1}.

surface

$$\mathcal{D} = \frac{\int E_z dA}{\int \|E\| dV} \tag{4.2}$$

which decreases by 4% when using a maximum element size of 0.1 μm compared to a size of 0.5 μm. This is important, as the coupling to the mechanical modes in the baseline model predominantly stems from the z-component of the electric field.

Maximum element size [m]	Eigenfrequency 1 [GHz]	Eigenfrequency 2 [GHz]
1.00E-07	6.4244	9.1391
2.00E-07	6.4377	9.1392
3.00E-07	6.4265	9.1391
4.00E-07	6.4435	9.1395
5.00E-07	6.4222	9.1391

Table 4.1: Frequency dependence of the electromagnetic solutions while varying the mesh density around the Josephson junction.

4.2 Comparison of simulation methods

4.2.1 Comparison between 2D and 3D simulations

COMSOL studies in three dimensions are computationally expensive. Therefore, simulations were also conducted in two dimensions to compare the accuracy and computation time. For this, axisymmetric simulations of the HBAR from the baseline model were set up. The results of the frequency domain studies conducted on the baseline model are shown in Figure 4.3. The computed frequency range is of 150 MHz (where the FSR is about 130 MHz) with a resolution of 50 kHz, and the applied load is Gaussian. Solid mechanics physics are solved without coupling, because the frequency domain studies are not yet feasible with coupled physics and the influence of the coupling is expected to be small. The resulting absolute frequencies of the fundamental modes and the FSR of both 2D and 3D simulations match very well. However, in the three-dimensional case, more modes are present and the spectrum seems more noisy. Reasons could be on one hand that the mesh needed for the additional dimension introduces artifacts in because it introduces new degrees of freedom, which has shown to impact the number of artifacts substantially, and on the other that in the 2D case we restrict the simulation to a fixed azimuthal mode number and are therefore only seeing a subset of eigenmodes.

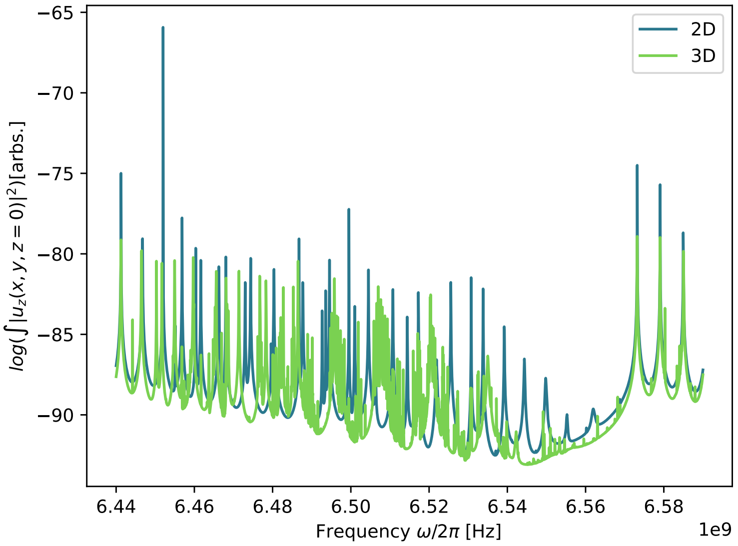

Figure 4.3: Solid mechanics spectra of the baseline model, simulated in both 2D and 3D. Perfect agreement is found for the FSR (from 6.44 GHz to 6.57 GHz) as well as for the transverse mode spacing of the first three modes. We observe less agreement for higher order modes and many more resonance frequencies in the 3D case.

4.2.2 Comparison between COMSOL and BeamProp

The results of COMSOL frequency domain simulations and the solutions of paraxial simulations with BeamProp are compared to each other in this section. The baseline model geometry is simulated in solid mechanics only, with a centered Gaussian driving load in two dimensions. The same geometry parameters (resonator length and dome shape) are used in the BeamProp simulations. The results are shown in Figure 4.4. The modes profiles that result from both simulations are of the family $LG(0,n), n \in \mathbb{N}$. The FSR from COMSOL is 138 MHz, while BeamProp simulations with 2000 round-trips result in a spectrum with an FSR of 137 MHz. In both methods, the transverse mode spacing between the fundamental and next higher mode is close to 5 MHz. Several things have to be noted:

- Only the first four modes agree well in frequency. The reason is the difference in TMS that adds up with increasing higher frequencies.
- The amplitudes of the modes in the spectrum computed in COMSOL are not monotonically decreasing, although there is a trend, whereas the ones from BeamProp are. This is more expected for the centered Gaussian drive applied, because higher order eigenmodes of the HBAR with spherical dome have a smaller mode overlap with it.
- Some peaks in the COMSOL spectrum appear as double peaks, as for example the fundamental mode at 5.9 GHz. There is no immediate explanation for this at the moment except for numerical errors.
- The spectra are are shifted with respect to each other in absolute frequency by 9.5 MHz for visual comparison.
- A last observation is that the transverse spacing is varying, and in particular, increases for the modes between 5.85 GHz and 5.875 GHz. Again, the transverse mesh density could be not high enough to resolve the modes correctly.

4.3 Diffraction loss

Loss estimation using boundary variation

To analyze the consistency of diffraction loss results that are computed by integrating the mechanical power flux that leaves the HBAR, solid mechanics simulations of the baseline model HBAR were conducted in two dimensions. The diffraction loss was then extracted for 200 eigenmodes found in a frequency range of 501 MHz, which covers three full FSRs. According to section 2.2.3, the quality factor associated with diffraction loss can be computed from the radially emitted power flux. Here, we varied the distance of the boundary at which the flux is evaluated from the symmetry axis of the HBAR between 60 μm and 90 μm, corresponding to 60% and 90% of the simulated HBAR radius

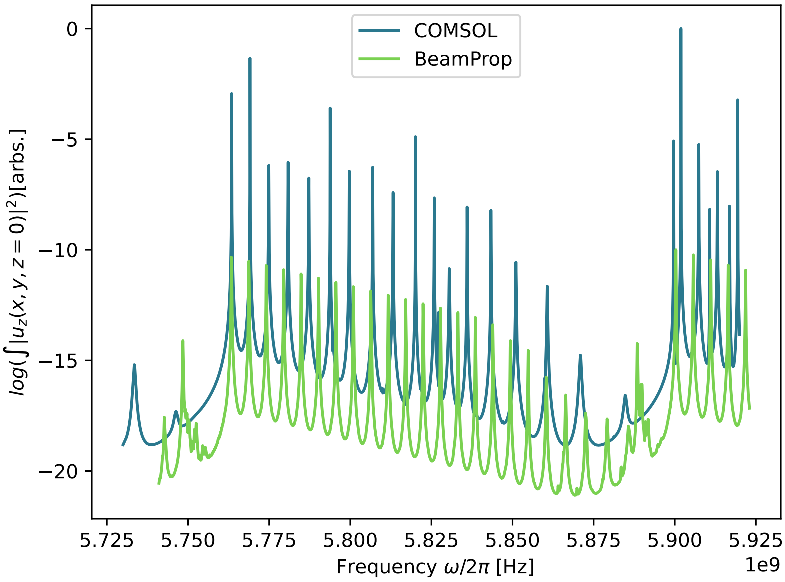

Figure 4.4: Comparison of the acoustic spectra computed in a COMSOL 2D frequency domain and the BeamProp method for the HBAR used in the baseline model. The BeamProp spectrum is shifted by +9.5 MHz to visually match both FSRs.

respectively. The results are shown in Figure 4.5. The quality factor of the fundamental mode at 6.573 GHz is consistently large, as is expected because fundamental modes are the most confined modes. However, other fundamental modes such as the one at 6.4412 GHz do not show this characteristic, i.e. their quality factor is small. It has to be concluded that with the transverse mesh density of the baseline model, further investigations are needed to increase the accuracy of diffraction studies. A possible explanation for the inconsistency could be that small numerical errors dominate at the boundaries because the mesh density in direction of the power flow is small at those boundaries.

4.4 Electromechanical coupling rates

4.4.1 Different dome shapes

The coupling rates were calculated for the lowest eigenmodes in the solid mechanics simulations for spherical, Gaussian and cosine dome types. The couplings are plotted as a function of eigenfrequencies of the modes in Figure 4.6. As expected, the differences are only minimal, since up to second order the surface profiles are matching. However, one observes a small shift in frequency of the Gaussian and cosine domes with respect to the

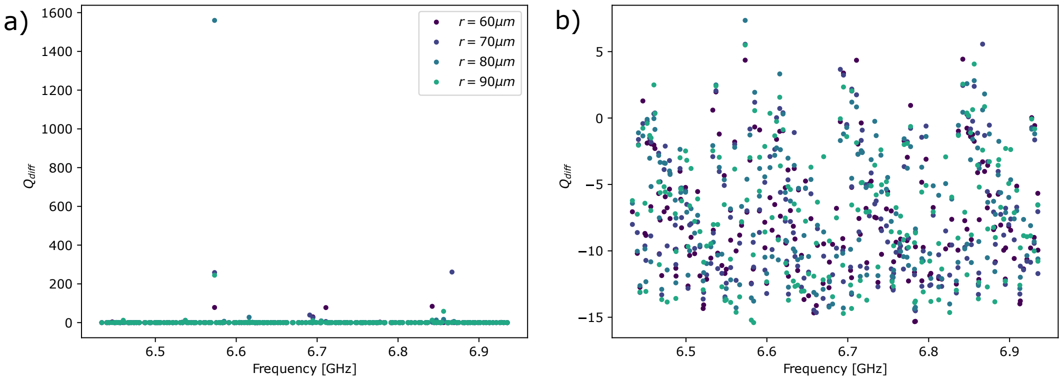

Figure 4.5: Analysis of the influence of the position of the boundary over which diffraction loss computation is evaluated over four FSRs in the baseline model HBAR. The fundamental mode at 6.573 GHz shows consistently a high quality factor. a) Diffraction quality factors. b) Logarithm of of the diffraction quality factors.

spherical. Furthermore, the results show that the coupling rate is potentially another characteristic that allows one to separate spurious from real modes, as a threshold at couplings of around 600 kHz would result in a good method for extracting the first four real eigenmodes. It is to be noted however, that for higher order modes, the couplings of real modes become comparable to spurious ones. An explanation of why spurious modes have smaller couplings could be that because of their random mode profiles, the overlap integral with the more slowly varying electric field profile becomes small.

4.4.2 Coupling to a ring antenna

Experiments were also conducted to investigate the antenna shape. For example, the baseline model was modified to have a ring-shaped antenna instead of a disk. The outer ring diameter was set to 20 μm. The result of this analysis is shown in Figure 4.7. The coupling rates are comparably higher than in samples in Ref. [35], which are in the order of 250 kHz, but a direct comparison can't be made because the baseline model has a gap of 3 μm and a substrate thickness of 40 μm, compared to 2 μm and 420 μm, respectively, of the sample.

4.5 Classification of spurious modes

Different methods for distinguishing computational artifacts from real modes in the results of eigenmode simulations were investigated. Examples include integrating the displacement fields of the eigenmodes in specific regions or surfaces, analysis of the Fourier

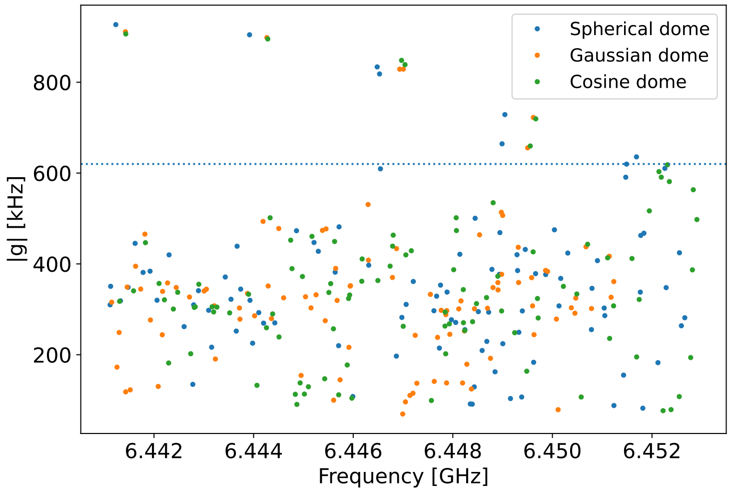

Figure 4.6: Couplings of the first few eigenmodes of the HBAR from the baseline model as well as of an equivalent Gaussian and cosine dome, as a function of their eigenfrequency. The dotted line is a guide to the eye separating LG(0,n) modes of the device (upper part) from computational artifacts (lower part).

transforms (to detect high frequency components) as well as image processing methods such as blob detection and convolutional neural networks. A simple measure based on the variance of the displacement field on the flat surface of the HBAR however performed very good, making it easy to classify the modes with a threshold. The result for the first 100 modes from an eigenmode simulation are shown in Figure 4.8. The reason for this is again the fact that the artifacts often have single points of large displacement, but otherwise are largely zero.

4.6 Radiation loss

Finally, a loss due to electromechanical coupling of the electric field of a qubit to phonons was investigated. Experimentally, the qubit T_1 coherence times in our group are typically tens of microseconds when measured without an HBAR bonded to it. This could be due to impurities introduce during fabrication, participation of additional surface in the field and radiation loss. A hint for this is that if the acoustic resonator is added, the coherence times or decay rates will depend on where the qubit frequency is placed with regard to the resonator spectrum. For a qubit decay measurement, the qubit frequency is Stark-shifted across the phonon modes of the attached HBAR. The result of a previous measurement and the fitted decay rates for each frequency are shown in Figure 4.9. One can observe an FSR of about 13.2 MHz and a transverse mode spacing of 1.2 MHz. Two main regions in the spectrum can be distinguished:

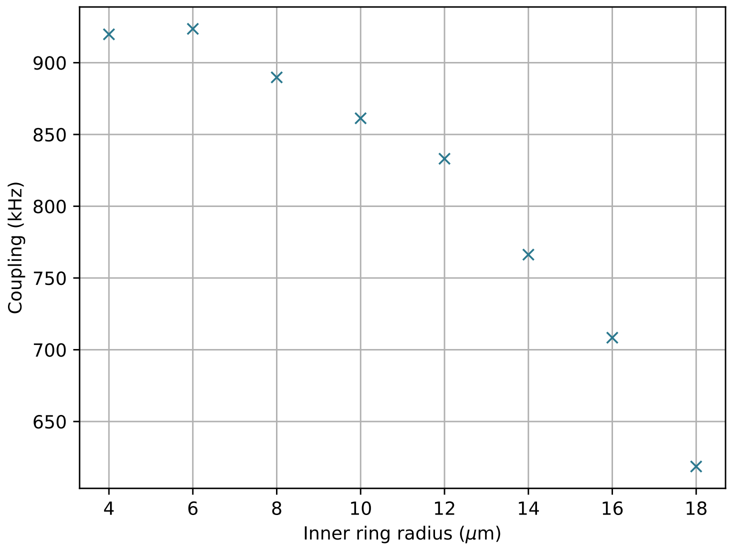

Figure 4.7: Coupling rates for a model with geometrical parameters as the baseline, but with an antenna with ring shape. The inner ring radius was varied, the outer ring radius was set to 20 μm. A full disk of 20 μm for the same model has a coupling rate of 927 kHz.

- The qubit frequency is on resonance with the fundamental phonon mode, or a next higher one. In this case, energy is coherently swapped between the qubit and the phonon mode, leading to (damped) Rabi oscillations.
- The second case is when the qubit frequency is off-resonance, typically at the end of the FSR. There, a qubit is not coupling to a specific phonon mode. However, the decay of the qubit in this frequency range is larger than the bare (unbonded) qubit decay.

Here, we present a model to estimate the qubit decay due to electromechanical loss, as described in Chapter 2.2.4. The spectrum and the density of phonon states of the HBAR were extracted from simulations of the acoustic Schrödinger equation. The spectrum is the direct result of the eigendecomposition. To get the density of states, the eigenfunctions are Fourier-transformed. In the one dimensional case, one can directly construct a density of states by assigning the transformed eigenstates to their eigenfrequency. The density of states in this case is shown in Figure 4.10. The range of the vertical axis is given by the depth of the potential well according to the acoustic Schrödinger equation and hence given in negative frequencies. Similarly to the density of states of a substrate with finite thickness but infinite extension in the other two dimensions, the energy as a function of wavevector shows a parabolic trend. In the two dimensional case, the density of states can be computed similarly from the eigenfunctions. For a density of states as

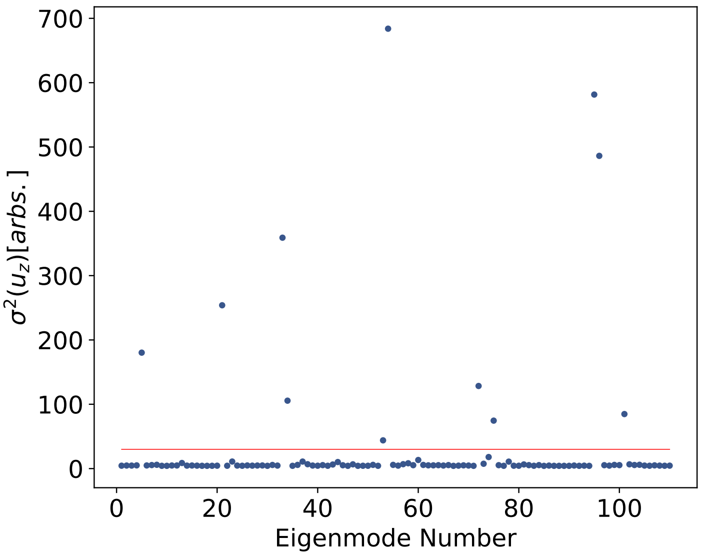

Figure 4.8: A simple measure to distinguish computational artifacts from physically plausible modes in COMSOL eigenmode simulations, based on the variance of the displacement fields. All modes above the threshold marked by the red line show low noise and Laguerre-Gaussian mode traits, while modes below are artifacts.

a function of the magnitude of the wavevector perpendicular to the flat surface of the HBAR, on can use the following computation method:

- Solve the Acoustic Schrödinger equation for the lowest n eigenfunctions
- Discretize the perpendicular wavevector $k_\perp^2 = k_x^2 + k_y^2$ in bins $k_{\perp,i}$, which can be saved in an array for each eigenfrequency
- For every eigenfrequency, Fourier-transform the degenerate eigenfunctions (modes), and for each, integrate their amplitude over the rings with center radius $k_{\perp,i}$ and thickness $t = k_{\perp,i} - k_{\perp,i-1}$. Add the result to bin i of the array corresponding to this eigenfrequency
- The density of states is then given by assigning these arrays to the closest frequency

In both the one dimensional and two dimensional case, the spectra are broadened with a heuristic lineshape, corresponding to a finite lifetime of the eigenstates in the resonator, a parameter that can be used to fit the model to experimental data. The second ingredient needed for the loss rate are the electric fields in the piezo-electric domes used to compute the coupling in k-space. They can be extracted from COMSOL eigenmode simulations, and this was done for different antenna radii ranging from 20 to 44 microns.

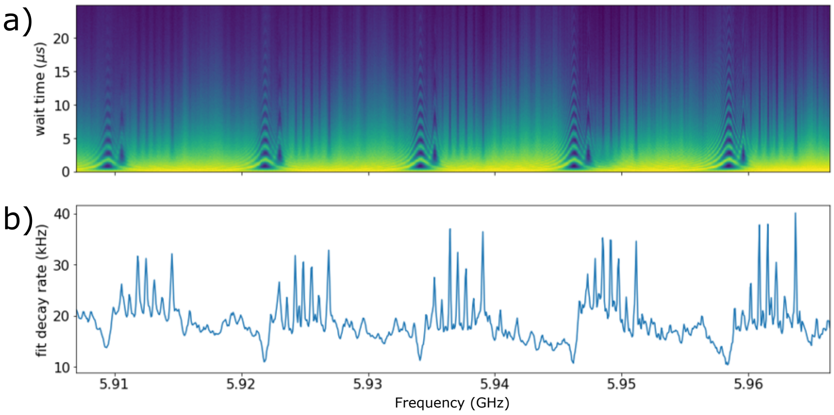

Figure 4.9: Measurement of the qubit decay and fitted decay rates. a) Chevron pattern produced by sweeping the qubit frequency across the phonon spectrum is shown. One sees four FSRs, with pronounced Rabi oscillations for the fundamental mode. b) For every frequency, an exponential decay is fitted for the wait time.

Under the assumptions mentioned in 2.2.4, we can compute the loss rates, which are proportional to the density of states multiplied by the Fourier transform squared of the electric field. This can be done by simple matrix multiplication (the overlap), the result of which, for an antenna of radius 20 μm and 44 μm can be seen in Figure 4.11. One can see that the size of the antenna may have a big influence on the qubit radiation loss, indicating that big antennas could reduce off-resonance decay rates. The peaks that can be seen result from the density of states at small values of k, since the Fourier transform of the electric field of a disk-shaped antenna results in a sinc-shaped coupling in k-space, which has a large magnitude at small values of k. A second interesting feature is the influence of the second and wider dome of the Hero sample. According to Figure 4.11, it contributes additionally to the decay for frequencies above -10 MHz. More importantly, one can see that the off-resonance region, the qubit decay baseline is smaller for larger antenna sizes because its Fourier transform is concentrated to smaller k values, and hence the overlap with the density of states contains less components from high k. This is the region thought to contribute to the off-resonance background.

In conclusion, this model provides us with a powerful tool which may allow us to minimize the loss rate depending on the geometry of the HBAR used, as well as to optimize the shape of the antenna which defines the electric field in the piezo-electric dome.

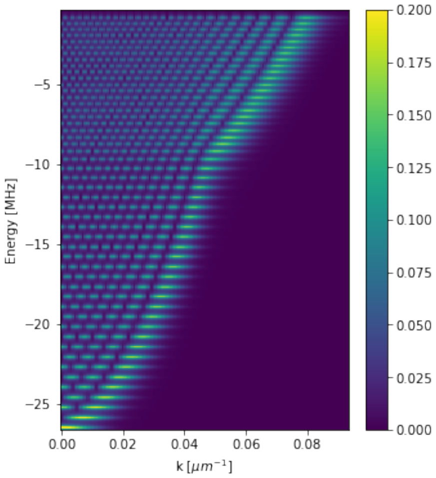

Figure 4.10: Density of states computed using the acoustic Schrödinger equation, used to compute the qubit loss rate. Horizontal lines correspond to the eigenfrequencies of the dome according to the analogy to a potential well, the lowest of which is the fundamental mode. The kink is introduced because the dome is composed of two sub-domes.

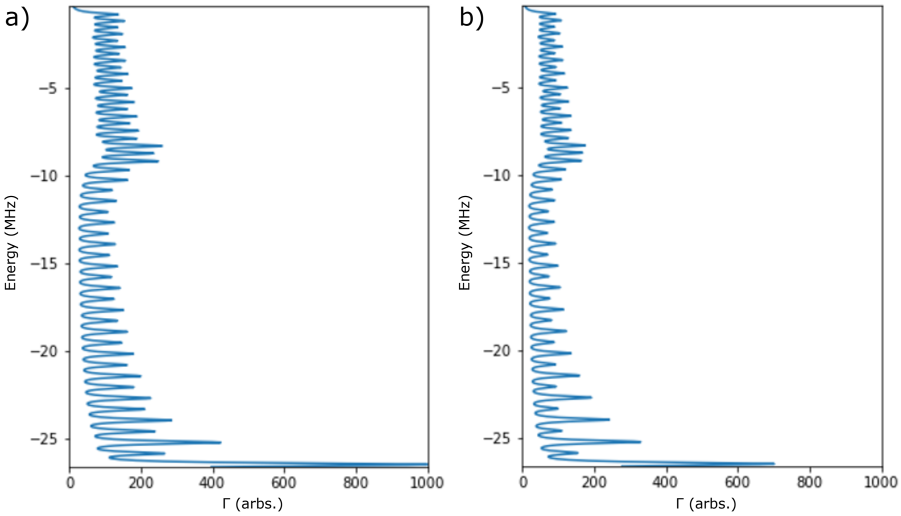

Figure 4.11: The qubit radiation loss was evaluated for different qubit antenna sizes. Two examples of loss patterns for an antenna with radius a) 20 μm and b) 44 μm are shown. The decay rate of the qubit is proportional to the overlap of the coupling and density of states. The main feature to observe is that the baseline (the decay rate around -15 MHz) is decreased for larger antennas.

Chapter 5

Outlook

5.1 COMSOL

Although the COMSOL simulations were improved to reduce the sensitivity to the mesh by an order of magnitude, the results of the COMSOL simulations also show that further efforts are needed. First, the diffraction loss accuracy could be improved by increasing the radial mesh density by an order of magnitude, but at the moment of writing such simulations are not feasible in three dimensions. Also, an open question remains whether the cylindrical offset of 0.15 μm separating the piezo-electric dome from the substrate can be avoided, since this prevents the implementation of arbitrary (realistic) dome shapes, albeit many alternative have already been explored. A last improvement to be done concerns the gap between the substrates. As the mesh density in z-direction of the HBAR in the baseline model required to resolve the eigenfrequencies accurately was only possible for a gap of at least 3 μm, some alternative mesh approaches have to be tried out to model smaller gaps.

5.2 Validation of loss model

There are a few next steps regarding the qubit decay rate model. First of all, the model requires more verification. This includes a closer analysis of the assumptions taken both in the derivation and on the computational side. Also, some consistency checks could be done, such as more variations of the dome shape and the antenna. Second, the model could be compared and fitted to measurements taken. Finally, there is a trade-off between the coupling rate and the qubit loss rate. As the electric field is increased for increasing coupling, the qubit decay rate will also increase. Instead of only optimizing the loss rate, one could try to minimize the product $g \cdot \Gamma$, to find the optimal balance for the specific hybrid quantum system $\hbar$BAR.

5.3 Phononic crystals

A very different and yet interesting approach for inhibiting qubit decay through phonon radiation may consist of creating a phononic crystal around the HBAR such that the relevant phonon frequencies fall into the bandgap of the crystal. This type of insulation has proven very effective in the context of optomechanical crystals. Furthermore, it may be possible to simulate such a device with similar geometry to the COMSOL models of the HBAR, as the number of degrees of freedom are not expected to grow too much because simulating a single layer of unit cells around the HBAR with appropriate periodic boundary conditions may be enough, allowing to predict the effectiveness before fabrication.

5.4 Mode selectivity engineering

For quantum information processing applications, it may be interesting to couple the qubit to the fundamental Laguerre-Gaussian mode only. As a result of the acoustic Schrödinger equation analogy (within its limitations), the spectrum of the HBAR only depends on the difference of the spatial profiles of the resonator surfaces. Therefore, one can in principle "cut out" pieces of the height profile of one surface and add it to the other without changing it. This could potentially allow the use of a mode matching surface (to the fundamental mode, which is Gaussian) on one side and a surface creating the resonator cavity on the other.

Chapter 6

Conclusion

In conclusion, methods for simulating a hybrid quantum system were evaluated, improved and extended, including classical multiphysics simulations which allow to reconstruct the quantum Hamiltonian with a previously developed hybrid quantization based on the eigenmode of the coupled system, as well as simulation methods for bulk acoustic wave resonator based on paraxial beam propagation. The key findings include the following:

- The accuracy of COMSOL Multiphyiscs simulations of the hybrid quantum system $\hbar$BAR was evaluated. This included a thorough analysis of the meshing process of the device, both in models in two and three dimensions. It was found that the previous mesh was highly sensitive to small changes of the mesh, and in particular the domain where solid mechanics was simulated required improvement. After their improvement, the results are more accurate by one order of magnitude.
- Frequency domain studies for different models of HBARs were implemented in COMSOL. This allows to extract the same spectra as can be done with an established Python library , which is based on the Fourier propagation of the paraxial limit. Good agreement both of the FSR and the TMS is found.
- Simulations of a novel type of ring-like antenna for the qubit in the $\hbar$BAR were used to estimate the reduction of the coupling rates to the HBAR showing a decrease of around 10% if the antenna ring has a inner diameter that is half of the outer diameter compared to a full disk. This is of importance because in future experiments for coherent transduction, optical fields may have to pass through such a ring-shaped antenna while mantaining large coupling rates.
- A method to estimate the qubit loss due to radiation decay was investigated. To this end, the density of phonon states in the acoustic resonator was extracted from the solutions of a Schrödinger equation describing the HBAR, and together with electric fields from COMSOL eigenmode simulations, the qubit decay rate was shown to decrease for increasing radius of the antenna.

Bibliography

1. O'Brien, J. L. Optical Quantum Computing. *Science* **318,** 1567–1570. eprint: `https://www.science.org/doi/pdf/10.1126/science.1142892`. `https://www.science.org/doi/abs/10.1126/science.1142892` (2007).
2. O'Brien, J. L., Furusawa, A. & Vučković, J. Photonic quantum technologies. *Nature Photonics* **3,** 687–695. ISSN: 1749-4893. `https://doi.org/10.1038/nphoton.2009.229` (Dec. 2009).
3. Chu, Y. *et al.* Quantum acoustics with superconducting qubits. *Science* **358,** 199–202. eprint: `https://www.science.org/doi/pdf/10.1126/science.aao1511`. `https://www.science.org/doi/abs/10.1126/science.aao1511` (2017).
4. Kloeffel, C. & Loss, D. Prospects for Spin-Based Quantum Computing in Quantum Dots. *Annual Review of Condensed Matter Physics* **4,** 51–81. eprint: `https://doi.org/10.1146/annurev-conmatphys-030212-184248`. `https://doi.org/10.1146/annurev-conmatphys-030212-184248` (2013).
5. Hong, S. *et al.* Nanoscale magnetometry with NV centers in diamond. *MRS Bulletin* **38,** 155–161 (2013).
6. Bruzewicz, C. D., Chiaverini, J., McConnell, R. & Sage, J. M. Trapped-ion quantum computing: Progress and challenges. *Applied Physics Reviews* **6,** 021314. eprint: `https://doi.org/10.1063/1.5088164`. `https://doi.org/10.1063/1.5088164` (2019).
7. Huang, H.-L., Wu, D., Fan, D. & Zhu, X. Superconducting quantum computing: a review. *Science China Information Sciences* **63,** 180501. ISSN: 1869-1919. `https://doi.org/10.1007/s11432-020-2881-9` (July 2020).
8. Sklan, S. R. Splash, pop, sizzle: Information processing with phononic computing. *AIP Advances* **5,** 053302. eprint: `https://doi.org/10.1063/1.4919584`. `https://doi.org/10.1063/1.4919584` (2015).
9. Wang, P. *et al.* Single ion qubit with estimated coherence time exceeding one hour. *Nature Communications* **12,** 233. ISSN: 2041-1723. `https://doi.org/10.1038/s41467-020-20330-w` (Jan. 2021).
10. Ballance, C. J., Harty, T. P., Linke, N. M., Sepiol, M. A. & Lucas, D. M. High-Fidelity Quantum Logic Gates Using Trapped-Ion Hyperfine Qubits. *Phys. Rev. Lett.* **117,** 060504. `https://link.aps.org/doi/10.1103/PhysRevLett.117.060504` (6 Aug. 2016).
11. Wang, C. *et al.* Towards practical quantum computers: transmon qubit with a lifetime approaching 0.5 milliseconds. *npj Quantum Information* **8,** 3. ISSN: 2056-6387. `https://doi.org/10.1038/s41534-021-00510-2` (Jan. 2022).

12. Andersen, C. K. *et al.* Repeated quantum error detection in a surface code. *Nature Physics* **16,** 875–880. ISSN: 1745-2481. `https://doi.org/10.1038/s41567-020-0920-y` (Aug. 2020).
13. De Neeve, B., Nguyen, T.-L., Behrle, T. & Home, J. P. Error correction of a logical grid state qubit by dissipative pumping. *Nature Physics* **18,** 296–300. ISSN: 1745-2481. `https://doi.org/10.1038/s41567-021-01487-7` (Mar. 2022).
14. Clerk, A. A., Lehnert, K. W., Bertet, P., Petta, J. R. & Nakamura, Y. Hybrid quantum systems with circuit quantum electrodynamics. *Nature Physics* **16,** 257–267. ISSN: 1745-2481. `https://doi.org/10.1038/s41567-020-0797-9` (Mar. 2020).
15. Manenti, R. *et al.* Circuit quantum acoustodynamics with surface acoustic waves. *Nature Communications* **8,** 975. ISSN: 2041-1723. `https://doi.org/10.1038/s41467-017-01063-9` (Oct. 2017).
16. Hann, C. T. *et al.* Hardware-Efficient Quantum Random Access Memory with Hybrid Quantum Acoustic Systems. *Phys. Rev. Lett.* **123,** 250501. `https://link.aps.org/doi/10.1103/PhysRevLett.123.250501` (25 Dec. 2019).
17. Kharel, P. *et al.* Ultra-high- Q phononic resonators on-chip at cryogenic temperatures. *APL Photonics* **3.** ISSN: 23780967. arXiv: `1803.10077`. `http://dx.doi.org/10.1063/1.5026798` (2018).
18. Blésin, T., Tian, H., Bhave, S. A. & Kippenberg, T. J. Quantum coherent microwave-optical transduction using high-overtone bulk acoustic resonances. *Phys. Rev. A* **104,** 052601. `https://link.aps.org/doi/10.1103/PhysRevA.104.052601` (5 Nov. 2021).
19. Balram, K. C. & Srinivasan, K. Piezoelectric Optomechanical Approaches for Efficient Quantum Microwave-to-Optical Signal Transduction: The Need for Co-Design. *Advanced Quantum Technologies* **5,** 2100095. eprint: `https://onlinelibrary.wiley.com/doi/pdf/10.1002/qute.202100095`. `https://onlinelibrary.wiley.com/doi/abs/10.1002/qute.202100095` (2022).
20. Carney, D. *et al.* Mechanical quantum sensing in the search for dark matter. *Quantum Science and Technology* **6,** 024002. `https://doi.org/10.1088/2058-9565/abcfcd` (Jan. 2021).
21. Forstner, S., Zych, M., Basiri-Esfahani, S., Khosla, K. E. & Bowen, W. P. Nanomechanical test of quantum linearity. *Optica* **7,** 1427–1434. `http://opg.optica.org/optica/abstract.cfm?URI=optica-7-10-1427` (Oct. 2020).
22. Bosman, S. J. *et al.* Multi-mode ultra-strong coupling in circuit quantum electrodynamics. *npj Quantum Information* **3,** 46. ISSN: 2056-6387. `https://doi.org/10.1038/s41534-017-0046-y` (Oct. 2017).
23. Nigg, S. E. *et al.* Black-Box Superconducting Circuit Quantization. *Phys. Rev. Lett.* **108,** 240502. `https://link.aps.org/doi/10.1103/PhysRevLett.108.240502` (24 June 2012).

24. Minev, Z. K. *et al.* Energy-participation quantization of Josephson circuits. *npj Quantum Information* **7,** 131. ISSN: 2056-6387. `https://doi.org/10.1038/s41534-021-00461-8` (Aug. 2021).
25. Wang, C. *et al.* Surface participation and dielectric loss in superconducting qubits. *Applied Physics Letters* **107,** 162601. eprint: `https://doi.org/10.1063/1.4934486`. `https://doi.org/10.1063/1.4934486` (2015).
26. McRae, C. R. H. *et al.* Materials loss measurements using superconducting microwave resonators. *Review of Scientific Instruments* **91,** 091101. eprint: `https://doi.org/10.1063/5.0017378`. `https://doi.org/10.1063/5.0017378` (2020).
27. *Springer Handbook of Condensed Matter and Materials Data* (eds Martienssen, W. & Warlimont, H.) `https://doi.org/10.1007/3-540-30437-1` (Springer Berlin Heidelberg, 2005).
28. Cleland, A. N. *Foundations of nanomechanics: from solid-state theory to device applications* (Springer Science & Business Media, 2013).
29. Kimel, I. & Elias, L. Relations between Hermite and Laguerre Gaussian modes. *IEEE Journal of Quantum Electronics* **29,** 2562–2567 (1993).
30. Galliou, S. *et al.* Extremely Low Loss Phonon-Trapping Cryogenic Acoustic Cavities for Future Physical Experiments. *Scientific Reports* **3,** 2132. ISSN: 2045-2322. `https://doi.org/10.1038/srep02132` (July 2013).
31. Cohen-Tannoudji, C., Diu, B. & Laloë, F. *Band 2* ISBN: 9783110638769. `https://doi.org/10.1515/9783110638769` (De Gruyter, Berlin, Boston, 2019).
32. Le Bellac, M. in *Quantum Physics* (ed Forcrand-Millard, P. d.) 455–506 (Cambridge University Press, 2006).
33. Marte, M. A. M. & Stenholm, S. Paraxial light and atom optics: The optical Schrödinger equation and beyond. *Phys. Rev. A* **56,** 2940–2953. `https://link.aps.org/doi/10.1103/PhysRevA.56.2940` (4 Oct. 1997).
34. Banderier, H. *Towards a hybrid EPR method for cQAD devices* MA thesis (ETH Zurich, 2021).
35. Von Lüpke, U. *et al.* Parity measurement in the strong dispersive regime of circuit quantum acoustodynamics. *Nature Physics* **18,** 794–799. ISSN: 1745-2481. `https://doi.org/10.1038/s41567-022-01591-2` (July 2022).
36. Newberry, B. P. & Thompson, R. B. A paraxial theory for the propagation of ultrasonic beams in anisotropic solids. *The Journal of the Acoustical Society of America* **85,** 2290–2300. eprint: `https://doi.org/10.1121/1.397775`. `https://doi.org/10.1121/1.397775` (1989).
37. Baer, M. *findiff Software Package* `https://github.com/maroba/findiff`. 2018. `https://github.com/maroba/findiff`.
38. Baltenkov, A. S. & Msezane, A. Z. Electronic quantum confinement in cylindrical potential well. *The European Physical Journal D* **70,** 81. ISSN: 1434-6079. `https://doi.org/10.1140/epjd/e2016-60728-2` (Apr. 2016).

ETH
Eidgenössische Technische Hochschule Zürich
Swiss Federal Institute of Technology Zurich

Declaration of originality

The signed declaration of originality is a component of every semester paper, Bachelor's thesis, Master's thesis and any other degree paper undertaken during the course of studies, including the respective electronic versions.

Lecturers may also require a declaration of originality for other written papers compiled for their courses.

I hereby confirm that I am the sole author of the written work here enclosed and that I have compiled it in my own words. Parts excepted are corrections of form and content by the supervisor.

Title of work (in block letters):

Optimization of phononic radiation loss patterns in a high overtone bulk acoustic resonator

Authored by (in block letters):

For papers written by groups the names of all authors are required.

Name(s):	**First name(s):**
Marti	Stefano

With my signature I confirm that

- I have committed none of the forms of plagiarism described in the 'Citation etiquette' information sheet.
- I have documented all methods, data and processes truthfully.
- I have not manipulated any data.
- I have mentioned all persons who were significant facilitators of the work.

I am aware that the work may be screened electronically for plagiarism.

Place, date

21.08.2022

Signature(s)

For papers written by groups the names of all authors are required. Their signatures collectively guarantee the entire content of the written paper.